SPANDIDOS PUBLICATIONS

Oxygen-sensing histone demethylase KDM6A modulates chondrocyte-to-osteoblast transdifferentiation by activating the Wnt/β-catenin pathway

YI RONG[1,2*], HAO YU[1*], HENG YIN[1,3], SHAOSHUO LI[1], JIANWEI WANG[1], ZHONGYUAN SHEN[4], XINXIN DING[1], FANCHEN BU[1], TIANYI DAI[1], GEAN WU[1] and ZHEN HUA[1,3]

[1]Department of Traumatology and Orthopedics, Wuxi Affiliated Hospital of Nanjing University of Chinese Medicine, Wuxi, Jiangsu 214071, P.R. China; [2]Department of Basic Medicine, School of Health Medicine, Wuxi Taihu University, Wuxi, Jiangsu 214063, P.R. China; [3]Jiangsu Chinese Medicine Clinical Innovation Center of Degenerative Bone and Joint Disease, Wuxi, Jiangsu 214071, P.R. China; [4]Department of Orthopedics, The Affiliated Hospital of Nanjing University of Chinese Medicine, Nanjing, Jiangsu 210029, P.R. China

Received July 30, 2025; Accepted February 20, 2026

DOI: 10.3892/ijmm.2026.5874

Abstract. Fracture healing is a complex biological process involving chondrocyte (CH) differentiation and endochondral ossification. A subset of CHs may transdifferentiate into osteoblasts, enhancing bone regeneration. The oxygen-sensing histone demethylase lysine demethylase 6A (KDM6A) and local oxygen microenvironment are hypothesized to serve pivotal roles in modulating this transition; however, the precise regulatory mechanisms remain unclear. To assess the role of KDM6A, an oxygen-sensitive histone demethylase, in endochondral ossification, an inducible cartilage-specific Kdm6a-knockout mouse model was generated. Single-cell RNA sequencing (scRNA-seq) analysis was performed in a mouse tibial fracture model to characterize CH subpopulations and their fate transitions during bone repair. scRNA-seq identified distinct CH subpopulations, including chondrocyte-derived osteoprogenitors (CDOPs), which acted as osteoblast precursors during endochondral ossification. Pseudotime trajectory analysis revealed a bifurcated differentiation pathway, with CDOPs exhibiting rapid osteoblast conversion. Functional enrichment analyses implicated the Wnt/β-catenin pathway in this transition. In vitro, CHs isolated from bone callus of KDM6A-knockout and control mice were induced to undergo transdifferentiation into osteoblasts under varying oxygen tensions. The expression levels of chondrogenic markers, osteogenic differentiation-related indicators and canonical Wnt signaling molecules, as well as the levels of histone dimethylation of H3K27 (H3K27me2) and trimethylation of H3K27 (H3K27me3) at their promoter regions, were assessed. *In vivo*, the molecular and functional consequences of KDM6A deficiency were characterized through histopathological evaluation and bone microarchitecture analysis. *In vitro*, CHs cultured under normoxic conditions exhibited greater osteogenic differentiation than those cultured under hypoxic conditions. Conversely, loss of KDM6A impaired the pro-osteogenic effect of normoxia on CH-to-osteoblast transdifferentiation, indicating the importance of KDM6A in oxygen-mediated CH-to-osteoblast transdifferentiation. Mechanistically, chromatin immunoprecipitation analysis revealed that under normoxic conditions, KDM6A-knockout CHs exhibited higher levels of the repressive histone marks H3K27me2 and H3K27me3 at the Wnt3a promoter region, as well as increased H3K27me3 levels at the Runt-related transcription factor 2 (RUNX2) promoter region, compared with control cells. These findings indicated that KDM6A catalyzed the removal of H3K27 methylation at the promoters of Wnt3a and RUNX2, thereby relieving their transcriptional repression. *In vivo*, KDM6A-knockout mice exhibited osteogenic defects and delayed fracture healing compared with control mice. KDM6A serves as a pivotal oxygen sensor that drives CH-to-osteoblast transdifferentiation and enhances fracture healing through Wnt/β-catenin pathway activation. The KDM6A-mediated oxygen response mechanism is a potential target for enhancing bone regeneration during fracture repair.

Correspondence to: Dr Zhen Hua or Dr Gean Wu, Department of Traumatology and Orthopedics, Wuxi Affiliated Hospital of Nanjing University of Chinese Medicine, 8 Zhongnan West Road, Wuxi, Jiangsu 214071, P.R. China
E-mail: wxzy044@njucm.edu.cn
E-mail: wga7025038@163.com

*Contributed equally

Key words: fracture healing, single-cell RNA sequencing, endochondral ossification, chondrocyte transdifferentiation, lysine demethylase 6A, Wnt/β-catenin pathway

Introduction

Bone fractures represent a significant global health burden, with an epidemiological study reporting >170 million new cases annually worldwide (1). While most fractures achieve successful healing, 5-10% result in delayed union or nonunion, creating substantial clinical and economic challenges (2). The

healing process is particularly compromised in anatomically vulnerable sites such as the tibia, where limited soft tissue coverage and poor vascularity frequently impede proper bone regeneration (3,4). The biological complexity of fracture repair is exemplified by the delicate balance between multiple cellular processes and molecular signaling pathways that must be precisely coordinated across temporal and spatial dimensions (5).

Fracture healing occurs via two primary mechanisms: Intramembranous ossification at the fracture margins and endochondral ossification in the central callus region (6,7). The latter process, which involves the formation of a cartilaginous template that is subsequently replaced by bone, is crucial for healing unsfig fractures and defects with limited stability (5,8). The traditional understanding was that hypertrophic chondrocytes (HTCs) in cartilaginous callus undergo apoptosis before bone formation (9-12). However, emerging evidence from lineage-tracing studies has fundamentally challenged this paradigm, demonstrating that a substantial proportion of HTCs can directly trans-differentiate into osteoblasts without undergoing programmed cell death (13-15). This newly recognized pathway contributes to bone regeneration, with a study indicating that 30-40% of osteocytes in the callus are derived from chondrocytes (CHs), reaching 80% at the chondroosseous junction (15).

The fracture microenvironment is characterized by dynamic physicochemical gradients, with oxygen tension representing a key regulatory signal (16,17). The initial hypoxic conditions within the avascular cartilaginous callus gradually transition to normoxic conditions through angiogenesis, creating a spatially and temporally heterogeneous oxygen landscape (18,19). While the hypoxia-inducible factor-1α (HIF-1α) pathway has been well-established as a mediator of cellular adaptation to low oxygen, promoting CH survival and angiogenesis (16,20,21), evidence suggests that more direct oxygen-sensing mechanisms operate at the epigenetic level to guide cell fate decisions (22,23). Histone modifications, particularly the methylation of histone H3 lysine 27 (H3K27), have emerged as critical epigenetic determinants of cellular differentiation (24,25). Trimethylation of H3K27 (H3K27me3), catalyzed by polycomb repressive complex 2, serves as a repressive mark that silences developmental genes (26), whereas demethylation by specific enzymes activates transcriptional programs (27).

Oxygen-sensitive histone demethylase lysine demethylase 6A (KDM6A) represents a compelling molecular link between microenvironmental cues and epigenetic regulation (22). Unlike HIF-1α, which primarily mediates adaptive metabolic responses, KDM6A directly senses oxygen levels through its Jumonji C (JmjC) domain and translates this information into epigenetic instructions by removing repressive H3K27 methylation marks (22,23). This unique property positions KDM6A as a potential key regulator of cell fate transitions in oxygen-gradient environments, such as fracture calluses. Supporting this notion, KDM6A has been shown to be essential for embryonic development (28,29) and serves critical roles in various differentiation processes, including the osteogenic differentiation of mesenchymal stem cells (30,31).

The Wnt/β-catenin signaling pathway has been established as a master regulator of osteoblastogenesis and fracture healing (32-35). Multiple studies have demonstrated that Wnt pathway activation enhances bone repair through various mechanisms, including the promotion of osteoblast differentiation and activity (36,37). Pharmacological approaches targeting negative regulators of this pathway, such as antibodies against sclerostin and Dickkopf-1, have shown promising results in accelerating bone regeneration in animal models (38-40). Wnt/β-catenin signaling has been specifically implicated in CH-to-osteoblast transdifferentiation, with a study showing that β-catenin stabilization in HTCs enhances their conversion into osteoblasts (41).

The convergence of oxygen sensing, epigenetic regulation and canonical signaling pathways presents a compelling framework for understanding the coordination of CH fate during bone repair. A study has established connections between KDM6A and Wnt signaling, with RNA sequencing analyses revealing effects on Wnt gene expression in KDM6A-deficient contexts (42). In bone marrow stromal cells, KDM6A directly removes H3K27me3 modifications from the promoter regions of osteogenic genes, including RUNX family transcription factor 2 (RUNX2), thereby initiating differentiation programs (30,31). However, to the best of our knowledge, the functional significance of this epigenetic regulator in fracture healing, particularly its role in integrating oxygen signals to modulate CH transdifferentiation via the Wnt/β-catenin pathway, remains unexplored.

Investigation of these mechanisms across different fracture types has revealed intriguing patterns of interaction. In tibial shaft fractures, where endochondral ossification predominates (43), the oxygen-KDM6A-Wnt axis may serve a particularly critical role because of the prolonged hypoxic conditions characteristic of these injuries (30,31,42). Conversely, in well-vascularized fracture sites or rigidly fixed fractures where intramembranous ossification predominates, the relative importance of this pathway may differ (22,23). Understanding these context-dependent variations is essential for the development of targeted therapeutic approaches.

Based on these considerations, we hypothesized that KDM6A serves as a critical molecular nexus, linking oxygen sensing to CH fate determination during fracture repair. Specifically, we hypothesized that, in the transitioning oxygen environment of the healing callus, KDM6A activation promotes CH-to-osteoblast transdifferentiation by removing repressive H3K27 methylation marks from Wnt pathway genes, thereby activating the Wnt/β-catenin/RUNX2 signaling axis. To test this hypothesis, an integrated approach combining single-cell RNA sequencing (scRNA-seq) of fractured calli, lineage tracing and cartilage-specific inducible Kdm6a-knockout was employed. This methodological framework was designed to uncover the mechanisms underlying the oxygen-dependent modulation of bone regeneration across different fracture environments and to assess its potential as a therapeutic target for challenging clinical scenarios, such as nonunions and osteoporotic fractures.

Materials and methods

Mice. All animal protocols were approved by the Animal Care and Use Committee of Wuxi Affiliated Hospital of Nanjing University of Chinese Medicine (approval

SPANDIDOS PUBLICATIONS

no. GZR2023032801; Wuxi, China). Mice were housed in groups of ≤5 animals in a room using microisolator technology, and kept at 22-24˚C with a 12-h light/dark schedule, with *ad libitum* access to food and water.

Kdm6a-Flox (a conditional knockout strain where essential exons of the Kdm6a gene are flanked by loxP sites), collagen type II α1 chain (Col2a1)-2A-tamoxifen (Tam)-inducible Cre recombinase (CreERT2) (expressing CreERT2 specifically in CHs, driven by the Col2a1 promoter) and R26-CAG-LSL-tdTomato (a Cre-dependent reporter strain in which a loxP-flanked transcriptional stop cassette prevents the expression of the tdTomato fluorescent protein; upon Cre-mediated recombination, tdTomato is expressed, permanently labeling Cre-active cells and their progeny) mice were purchased from Shanghai Model Organisms Center, Inc. All mutant mice had a C57/B6J background. Col2a1-2A-CreERT2 mice were bred with R26-CAG-LSL-tdTomato mice to generate inducible cartilage-specific labeled mice that carried a Tam-inducible CreERT2 transgene under the control of the Col2a1 gene promoter for CH-specific expression, and the Cre/loxP-inducible Rosa-CAG-LSL-tdTomato reporter to mark the cells after CreER activity was induced by Tam injections. To generate inducible cartilage-specific Kdm6a-knockout mice, $Kdm6a^{flox/flox}$ mice were bred with Col2a1-2A-CreERT2&R26-CAG-LSL-tdTomato mice to generate $Kdm6a^{flox/+}$&Col2a1-2A-CreERT2&R26-CAG-LSL-tdTomato (fx/wt) mice, and these mice were intercrossed or bred with $Kdm6a^{flox/flox}$ mice again to generate $Kdm6a^{flox/flox}$& Col2a1-2A-CreERT2&R26-CAG-LSL-tdTomato (fx/fx) mice and fx/wt mice (44). Fx/wt mice were used as controls. DNA was obtained from tail biopsy samples and genotyping was performed using PCR (2X Taq Plus Master Mix; P212; Vazyme Biotech Co., Ltd.). The conditions for amplification reactions were as follows: 94˚C for 3 min, followed by 34 cycles of 94˚C for 30 sec, 56˚C (Kdm6a-Flox and Col2a1-CreERT2)/58˚C (R26-CAG-LSL-tdTomato) for 30 sec and 72˚C for 30 sec. The primer sequences are shown in Table SI. The PCR products were separated on a 3% agarose gel, stained with GelStain fluorescent nucleic acid dye (TransGen Biotech Co., Ltd.) and visualized using a fully automatic digital gel imaging analysis system (Tanon Science and Technology Co., Ltd.). As described in Data S1, an example of mouse tail clipping PCR genotype identification results is shown in Fig. S1. A total of 120 male mice were used in the present study. At the start of the experiment, the mice were 6 months old, with body weights ranging between 25 and 30 g. According to their genotype, the mice were divided into two groups: The inducible cartilage-specific Kdm6a-knockout group (fx/fx; n=60) and the control group (fx/wt; n=60). Mice from each group were then randomly allocated to different experimental endpoints as follows: scRNA-seq (n=6 per genotype), histological staining (n=15 per genotype), radiological examination (n=6 per genotype) and cytological experiments (n=33 per genotype). After the primary CHs were extracted from the mouse cartilage callus, KDM6A protein expression in the cells of the two groups was detected by western blotting to verify successful gene knockout (Fig. S2). Live-cell imaging was performed during the *in vitro* induction of CH transdifferentiation into osteoblasts in the cartilage callus. Imaging was performed directly after transferring the cells into osteogenic induction culture medium. A fluorescence microscope (Carl Zeiss AG) equipped with an environmental control chamber was used to maintain the cells at 37˚C with 5% CO_2 during observation. Imaging was performed for 48 h, capturing an image every 30 min. Fluorescence imaging showed that the CHs specifically expressed a clear red labeling signal, and the Col2a1-CreERT2/RosatdTomato model was successfully established (Fig. S3).

Tibial fracture model. Fx/fx and fx/wt mice were intraperitoneally injected with 75 mg/kg Tam (Sigma-Aldrich; Merck KGaA) once daily for 5 days. The fracture model was established on the second day after induction. Mice were weighed and anesthetized by intraperitoneal injection of 0.4% pentobarbital sodium at a dose of 40 mg/kg. After the mice were completely anesthetized, the skin was prepared in front of the left tibia, and hair was removed as cleanly and thoroughly as possible. Mice were placed in the left lateral position. The surgical site on the left lower limb was disinfected three times with iodine, followed by draping with sterile fenestrated drapes. Using high-temperature and high-pressure sterilized instruments, a small incision of ~1 cm was made along the longitudinal axis of the left tibia, from the knee joint to the middle section of the tibia. Hemostatic forceps were used to expose the anterior edge of the tibia to obtain the skin, muscles and fascia. Surgical blade 11 was positioned at the highest point of the anterolateral protrusion of the tibia. A transverse fracture was created by striking the base of the blade vertically with a small hammer and a slight lateral movement was performed to confirm the fracture. A sterile 1-ml syringe needle was inserted into the medulla for fixation, and the exposed needle was removed (45). After disinfection with Aner iodine, the incision was sutured layer-by-layer using a 5-0 medical suture needle and thread. After the operation, 40,000 U penicillin was injected intramuscularly for 3 consecutive days to prevent infection. The mice were raised without any activity restrictions. The incision conditions and activity of the mice were monitored daily. Fractured callus tissues were harvested on days 10 and 21 post-fracture for single-cell sequencing. The samples at each time point were obtained from 6 different mice. Samples of the left tibiae from 12, 12 and 18 different mice were collected on days 10, 21 and 28 post-fracture for radiological and histological analyses.

scRNA-seq. Bone callus samples were dissociated into single-cell suspensions. The cell concentration and viability were determined using a Countstar Rigel S2 automated cell fluorescence analyzer (Shanghai Ruiyu Biotech Co., Ltd.) with AO/PI staining (RE010212; Shanghai Ruiyu Biotech Co., Ltd.) and Countstar counting slides (CO010101; Shanghai Ruiyu Biotech Co., Ltd.). The concentration was adjusted to 700-1,200 cells/μl. Single-cell capture, barcoding and library preparation were performed using the Chromium Next GEM Single Cell 3' Reagent Kits v3.1 (cat. no. 1000268; 10x Genomics). Cell suspensions were combined with barcoded gel beads and master mix, and encapsulated into gel beads-in-emulsion (GEMs) using a microfluidic system. Within the GEMs, poly (dT) primers bound to mRNA poly-A tails to initiate reverse transcription (RT). Full-length barcoded cDNA was generated by

RT using the integrated RT reagents: RT Reagent B (cat. no. 2000165; buffer), RT Enzyme C (M-MLV Reverse Transcriptase; cat. no. 2000085/2000102), Template Switch Oligo (cat. no. 3000228) and Reducing Agent B (cat. no. 2000087) from the Chromium Next GEM Single Cell 3' Reagent Kit v3.1 (10x Genomics). The RT reaction was performed at 53˚C for 45 min, followed by enzyme inactivation at 85˚C for 5 min. The GEMs were then broken, and the pooled cDNA was amplified by PCR using a high-fidelity DNA polymerase from the Amp Mix (cat. no. 2000047/2000103; 10x Genomics) with the following primers: Forward, 5'-CTACACGACGCTCTTCCGATCT-3' and reverse, 5'-AAGCAGTGGTATCAACGCAGAG-3'. The thermocycling conditions were as follows: 98˚C for 3 min; cycling (12-13 cycles, optimized for cell recovery) at 98˚C for 15 sec, 63˚C for 20 sec and 72˚C for 1 min; and 72˚C for 1 min. The quality and size distribution of the amplified cDNA were verified using an Agilent 2100 Bioanalyzer (Agilent Technologies, Inc.), showing a main peak of 1,000-2,000 bp. The cDNA was fragmented (~400 bp on average) and sequencing adapters were added. A final sample indexing PCR was conducted using the same Amp Mix and the Dual Index Kit TT Set A primers (cat. no. 1000215; 10x Genomics) containing unique i5 and i7 index sequences. The sequences were: P5 primer (with i5 index), 5'-AATGATACGGCGACCACCGAGATCTAC AC-N10-ACACTCTTTCCCTACACGACGCTC-3'; P7 primer (with i7 index), 5'-CAAGCAGAAGACGGCATACGA GAT-N10-GTGACTGGAGTTCAGACGTGT-3' (where N10 represents the unique 10-bp index sequence for each sample). The indexing PCR conditions were: 98˚C for 45 sec; cycling (8-16 cycles, optimized for cDNA input) at 98˚C for 20 sec, 54˚C for 30 sec and 72˚C for 20 sec; and 72˚C for 1 min. The concentration of the final sequencing library was determined by quantitative PCR (qPCR) to ensure accurate loading for sequencing. The quantification was performed using the VAHTS Library Quantification Kit for Illumina® (cat. no. NQ101; Vazyme Biotech Co., Ltd.) according to the manufacturer's protocol. The fluorescent dye premix solution and the primers (forward, 5'-AAT GATACGGCGACCACCGA-3'; reverse, 5'-CAAGCAGAA GACGGCATACGA-3') were all included in this kit. This method provides absolute quantification of the library. Briefly, a dilution series of the library was prepared and used as template alongside the DNA standards (cat. no. NQ105; Vazyme Biotech Co., Ltd.) to generate a standard curve. Each qPCR reaction was set up in triplicate using the provided premix. Amplification was carried out on a qPCR instrument with a standard cycling protocol appropriate for the kit (95˚C for 5 min, followed by 35 cycles of 95˚C for 30 sec and 60˚C for 45 sec). The library concentration was calculated according to the kit's protocol. A standard curve was generated using the provided DNA standards of known concentrations. The Ct values of the library samples were interpolated from this standard curve to obtain a preliminary concentration. This value was then corrected for the average library length using the following formula: Corrected concentration (pM)=[452 bp/mean library length (bp)] x preliminary concentration (pM). The final, accurate concentration of the original library (nM) was derived by multiplying the corrected concentration by the dilution factor. Following quantification, the pooled libraries were diluted to a final concentration of 200 pM and loaded onto an Illumina NovaSeq 6000 flow cell (Illumina, Inc.) for cluster generation and sequencing. Paired-end 150-bp sequencing was performed on an Illumina NovaSeq 6000 platform (Illumina, Inc.) using the Illumina NovaSeq 6000 S4 Reagent Kit (cat. no. 20028312; Illumina, Inc.). Raw sequencing data were processed using CellRanger (v8.0.1; 10x Genomics). Downstream analysis was performed in R (v4.1.2; https://www.r-project.org/) utilizing the Seurat package (v4.1.1; https://satijalab.org/seurat/).

The raw sequencing data were processed using CellRanger for genome alignment, background cell filtering and unique molecular identifier (UMI) counting of cellular transcripts. Data integration across multiple samples was performed using the anchor-based canonical correlation analysis method as previously described (46). For the cell gene expression matrix generated by CellRanger, Seurat software was used to filter dead or stressed cells by removing cells with abnormal gene or UMI counts, high mitochondrial gene content and potential doublets. The filtering criteria were set as follows: Number of genes per cell, 500-infinity; total UMIs per cell, < infinity; and proportion of mitochondrial gene expression per cell, <25%; and doublets were removed using the DoubletFinder package (version 2.0.4; https://github.com/chris-mcginnis-ucsf/DoubletFinder). The distribution of basic information of each sample cell after cell filtering is shown in Figs. S4 and S5.

After quality control, only the high-quality cells suitable for downstream analyses were retained (Data S1; Tables SII and SIII). During data preprocessing, regression analysis was performed to eliminate the effects of total UMI counts and mitochondrial gene proportion, and expression data were normalized using a scale factor of $1x10^4$. Highly variable genes were selected using the FindVariableGenes algorithm in the Seurat package (parameters: x.low.cutoff, 0.0125; y.cutoff, 0.5), and principal component analysis (PCA) was performed based on these genes. The top 100 significant principal components were selected, and cell sub-clusters were identified using the FindClusters function (derived from Seurat v4.1.1; dims, 1:30; resolution, 0.5). Finally, uniform manifold approximation and projection (UMAP) was employed for dimensionality reduction and visualization of the gene expression data.

Following cell clustering and annotation, the expression patterns of key marker genes across subpopulations were visualized. UMAP plots depicting the expression of individual genes were generated using the FeaturePlotfunction in Seurat, where color intensity corresponds to the expression level of the feature gene in each cell. Violin plots were used to display the distribution of expression for these marker genes across the annotated cell clusters. Additionally, a dot plot was created to summarize the expression of characteristic marker genes across the main CH-osteoblast lineage subpopulations. In this plot, the size of the dot represents the percentage of cells within a cluster expressing the gene, and the color gradient indicates the mean expression level.

Based on marker genes and referencing the CellMarker2.0 database (http://117.50.127.228/CellMarker/), cell type

annotation was performed. For enrichment analysis, genes with specific high expression in each cell subcluster (top 10) were subjected to Gene Ontology (GO) and Kyoto Encyclopedia of Genes and Genomes (KEGG) pathway enrichment analysis using the clusterProfiler R package (v4.2.2; https://bioconductor.org/packages/clusterProfiler) to interpret potential biological functions. The enrichment results were visualized using the ggplot2 package (v3.4.0; https://cran.r-project.org/web/packages/ggplot2/index.html), with bubble plots and bar charts displaying significantly enriched pathways. Gene set enrichment analysis (GSEA) was conducted using GSEA software (v4.4.0; https://www.broadinstitute.org/gsea/), and the results were visualized using the GseaVis R package (v0.1.1; https://github.com/junjunlab/GseaVis).

Pseudotime trajectory analysis of CH-to-osteoblast transdifferentiation. Pseudotime trajectories were constructed by integrating highly variable genes from cell subpopulations using Monocle3 (v1.3.4; http://cole-trapnell-lab.github.io/monocle3/). Trajectory visualization was achieved in combination with UMAP. The learn-graph algorithm was employed to define CHs as the root of the trajectory, and dynamic changes in gene expression along pseudotime were analyzed using the plot-genes-in-pseudotime function.

CellChat-based cell-cell communication analysis. The dataset was analyzed using the CellChat package (version 2.1.2; https://github.com/sqjin/CellChat) in R (version 4.4.1; https://www.r-project.org/). CellChat models the intercellular communication probability by applying the law of mass action and integrating gene expression data with prior knowledge of the interactions among signaling ligands, receptors and their cofactors. Based on cell type annotation and identification of upregulated genes, the computeCommunProb function was used to infer ligand-receptor interaction probabilities, the computeCommunProbPathway function was used to quantify pathway-level communication strength and key interactions were visualized as chord diagrams using the netVisual-chord-gene function.

H&E and safranin O-Fast Green staining. After fixation in 4% paraformaldehyde at room temperature for 24 h, the samples were decalcified in an EDTA decalcification solution at room temperature. The decalcification solution was changed every 2-3 days. During each solution change, the progress of decalcification was assessed by testing the tissue firmness. Decalcification was considered complete when a 1-ml syringe needle could be inserted into the tibial cortex without resistance. Once decalcification was complete, tibial specimens were rinsed under running water for 4 h, dehydrated, cleared, embedded in paraffin and sectioned. The thickness of sections was 3 μm. The sections were stained with H&E (Beijing Solarbio Science & Technology Co., Ltd.) using hematoxylin solution for 5 min and eosin solution for 1 min, and safranin O-Fast Green (Wuhan Servicebio Technology Co., Ltd.) using Fast Green for 5 min followed by Safranin O for 2 min according to the manufacturer's instructions at room temperature. Images were acquired using a panoramic digital slide scanner (3DHISTECH, Ltd.), which is a high-resolution whole-slide imaging system based on bright-field light microscopy.

Immunofluorescence staining. The sample fixation and decalcification steps were the same as those for H&E and safranin O-Fast Green staining. The thickness of paraffin sections was 3 μm. The paraffin sections were placed one by one into xylene I and xylene II for dewaxing for 10 min each, then soaked in absolute ethanol I and absolute ethanol II for 5 min each, rehydrated in 95, 85 and 75% ethanol for 3 min each, and finally rinsed in distilled water for 2 min. Subsequently, the paraffin sections were immersed in a 1X antigen retrieval solution and heated at 100˚C for 20 min. After cooling to room temperature, the sections were washed with PBS. Permeabilization was performed by incubating the tissues with Triton X-100 (ready-to-use working solution; cat. no. P0096; Beyotime Biotechnology) for 30 min, followed by incubation with 3% BSA (Beijing Biosynthesis Biotechnology Co., Ltd.) at room temperature for 30 min to block nonspecific binding. The sections were then incubated overnight at 4˚C with diluted primary antibody [anti-osteocalcin (OCN); 1:400; cat. no. ER1919-20; Hangzhou HuaAn Biotechnology Co., Ltd.] After washing with PBS, the sections were incubated with a fluorescent secondary antibody [anti-rabbit IgG (H+L), F(ab')2 Fragment; Alexa Fluor® 488 Conjugate; 1:1,000; cat. no. 4412; Cell Signaling Technology, Inc.] in the dark at room temperature for 50 min. After washing with PBS, the nuclei were counterstained with DAPI at room temperature for 10 min. Fluorescence images were acquired using a panoramic digital slide scanner, and analyzed using ImageJ software (1.54p; National Institutes of Health).

CH isolation from the fracture callus. On day 10 after modelling, CHs were isolated from the fracture calli of the mice. The mice were euthanized by cervical dislocation, and the left lower limb was removed and placed in a pre-chilled culture dish containing PBS supplemented with penicillin-streptomycin at a 1:9 ratio. Using sterilized instruments, the skin was incised at the knee joint, and the surrounding hair, muscle, fascia and vascular tissues were carefully separated to expose the fracture site. The cartilaginous callus was isolated from the surrounding fibrous tissue, and translucent cartilage was scraped off using a blade, taking care to remove cortical bone and other bony tissues. A randomly selected piece of the removed cartilage tissue was subjected to Alcian blue and Alizarin red combined staining (data not shown) to ensure that the cartilage tissue collected did not contain bone tissue. Briefly, the tissue fragment was fixed in 4% paraformaldehyde at 4˚C for 24 h, embedded in paraffin and sectioned at 4 μm thickness. Sections were stained with Alcian Blue (pH 2.5) for 30 min and Alizarin Red S solutions for 5 min at room temperature according to standard protocols, and observed under a light microscope (Olympus BX53; Olympus Corporation).

The collected cartilage was placed in a pre-chilled culture dish containing PBS with penicillin-streptomycin (1:9 ratio) and kept on ice. The cartilage was cut into small fragments of ~1 mm using fine scissors, and the cartilage fragments were transferred into a 15-ml centrifuge tube.

Subsequently, 4 ml of 0.25% trypsin-EDTA solution was added and the sample was incubated at 37˚C for 15 min to remove any attached fibroblasts or osteoblasts. During digestion, the tube was manually shaken for 15 sec every 5 min to ensure complete digestion. The digestion was

terminated by adding 4 ml complete CH medium [10% FBS (Sigma-Aldrich; Merck KGaA), 1% penicillin-streptomycin and 89% DMEM/F12 (1:1) (HyClone; Cytiva)], and the sample was centrifuged at 200 x g at 4˚C for 5 min. The supernatant was discarded and the tissue was washed twice with PBS.

A mixture of 1 ml hyaluronidase (1 mg/ml; ~400 U), 1 ml collagenase IA (2 mg/ml; >250 U) and 1 ml DNase II (0.25 mg/ml; >250 U) was prepared, and 3 ml of this enzyme mixture was added to the tissue. The samples were digested at 37˚C for 30 min in an incubator. Digestion was terminated by adding 3 ml complete CH medium, and the sample was centrifuged at 200 x g at 4˚C for 5 min. The supernatant from the first 30-min digestion was discarded to remove remaining fibroblasts and osteoblasts.

A new aliquot (3 ml) of the enzyme mixture was then added, and the tissue was digested for an additional 30 min at 37˚C. After adding 3 ml complete medium to terminate digestion and allowing the cartilage to settle, the supernatant was collected and filtered through a 70-μm cell strainer, followed by centrifugation at 200 x g at 4˚C for 5 min. The supernatant was removed and the cell pellet was gently resuspended in 1 ml complete CH medium.

This process of enzymatic digestion, centrifugation and cell collection was repeated with a freshly prepared enzyme mixture until all CHs were released, as indicated by the absence or minimal presence of cell pellets in the centrifuge tube after spinning the supernatant from the digestion. This protocol can yield highly purified cartilage cell preparations characterized by strong expression of cartilage formation markers and a strong tendency for cells to synthesize a cartilage matrix rich in proteoglycans (47).

Hypoxic culture and osteogenic induction. After CHs isolated from the fracture callus in both groups of mice had established stable growth to the appropriate size and density under hypoxic conditions (6% O_2), the cells were randomly divided into four groups: fx/wt hypoxia group (continued culture in 6% O_2), fx/wt normoxia group (cultured in 21% O_2), fx/fx hypoxia group (continued culture in 6% O_2) and fx/fx normoxia group (cultured in 21% O_2). The oxygen concentrations of 6 and 21% were selected based on the established oxygen-sensing property of KDM6A. A seminal study demonstrated that the enzymatic activity of its JmjC domain was inhibited below ~5% O_2 (22). Therefore, 6% O_2 represents a point where activity potentially begins to recover, while 21% O_2 (atmospheric level) reflects its fully active state. This range allows interrogation of the functional continuum of KDM6A from inhibition to full activation, thereby enabling a clear analysis of the axis linking oxygen levels, KDM6A-mediated epigenetic regulation and cell fate.

The original CH culture medium [10% fetal bovine serum, 1% penicillin-streptomycin and 89% DMEM/F12 (1:1)] was replaced with osteogenic induction medium [α-Minimum Essential Medium (HyClone; Cytiva) supplemented with 10% fetal bovine serum, 1% L-glutamine, 1% penicillin-streptomycin, 10 mM β-glycerophosphate, 0.2 mM ascorbate-2-phosphate and 100 ng/ml bone morphogenetic protein 2 (BMP-2)] to induce the transdifferentiation of CHs into osteoblasts at 37˚C for 7 days. The culture medium was replaced every 2-3 days.

Alcian blue, alizarin red and alkaline phosphatase (ALP) staining. After 7 days of osteogenic induction, the cells seeded in 24-well plates ($2.5x10^4/cm^2$) were removed from the incubator. The culture medium was discarded and the cells were washed with PBS and fixed with 4% cell fixative (P1110; Beijing Solarbio Science & Technology Co., Ltd.) at room temperature for 15 min. According to the manufacturer's protocols, staining was performed as follows: Alcian blue (E670107; Sangon Biotech Co., Ltd.) staining for 30 min at room temperature, ALP (G1481; Beijing Solarbio Science & Technology Co., Ltd.) staining for 2 h at 37˚C and Alizarin red (G1038; Wuhan Servicebio Technology Co., Ltd.) staining for 30 min at room temperature. Images were observed under a light microscope and analyzed using ImageJ software (1.54p; National Institutes of Health).

RT-qPCR. Total mRNA was extracted from each cell sample using TRNzol reagent (Tiangen Biotech Co., Ltd.), and cDNA was obtained by RT using the PrimeScript™ FAST RT reagent Kit with gDNA Eraser (Takara Bio, Inc.) according to the manufacturer's instructions. Reverse-transcribed cDNA was used as the template, and primers and TB Green Premix Ex Taq II (Tli RNaseH Plus) (Takara Bio, Inc.) were added to perform qPCR. The amplification reaction conditions were as follows: 95˚C for 30 sec, followed by 40 cycles of 95˚C for 5 sec and 60˚C for 34 sec. Finally, β-actin was used as an internal reference, and the relative expression levels of the target genes were calculated using the $2^{-\Delta\Delta Cq}$ method (48). The mRNA levels of Col2a1, collagen type X α1 chain (Col10a1), aggrecan (Acan), collagen type I α1 chain (Col1a1), secreted phosphoprotein 1 (Spp1), secreted protein acidic and cysteine rich (Sparc) and β-actin were analyzed using the primer sequences listed in Table I.

Western blotting. The protein extraction buffer was prepared with a ratio of RIPA lysis buffer (Jiangsu Kangwei Century Biotechnology Co., Ltd.) to proteinase inhibitor mixture (Jiangsu Kangwei Century Biotechnology Co., Ltd.) of 100:1. Cells were lysed in the protein extraction buffer on ice for 20 min to extract protein samples. When analyzing dimethylation of H3K27 (H3K27me2) and H3K27me3, nuclear lysates were prepared using the Nuclear and Cytoplasmic Protein Extraction Kit (P0028; Beyotime Biotechnology), with histone H3 serving as the nuclear reference. The protein concentration was determined using the BCA method. Equal amounts (20 μg/lane) of protein were loaded onto a sodium dodecyl sulfate-polyacrylamide gel (4-12%) for electrophoresis. After electrophoresis, the proteins were transferred to a PVDF membrane, and the membrane was blocked with a protein-free rapid blocking solution (Boster Biological Technology) at room temperature for 10 min. Primary antibodies, including anti-KDM6A antibody (1:1,000; cat. no. 33510; Cell Signaling Technology, Inc.), anti-Wnt3a antibody (1:1,000; cat. no. 2391; Cell Signaling Technology, Inc.), anti-β-catenin antibody (1:1,000; cat. no. 37447; Cell Signaling Technology, Inc.), anti-RUNX2 antibody (1:1,000; cat. no. ab236639; Abcam), anti-GAPDH antibody (1:2,000; cat. no. ab8245; Abcam), anti-histone H3 (di methyl K27) antibody (1:1,000; cat. no. 9728; Cell Signaling Technology, Inc.), anti-histone H3 (tri methyl K27) antibody (1:1,000; cat. no. 9733; Cell Signaling

SPANDIDOS PUBLICATIONS

Table I. Nucleotide sequences of primers used for reverse transcription-quantitative PCR.

Target gene	Forward primer (5'-3')	Reverse primer (5'-3')
Col2a1	AGAGGGGACTGAAGGGACACC	GCCAGGGATTCCATTAGAGCC
Col10a1	GCTGCCTCAAATACCCTTTCTGC	GGAATGCCTTGTTCTCCTCTTACTG
Acan	TAGAACCCTCGGGCAGAAGAAAG	CTGTAGCCTGTGCTTGTAGGTGTTG
Col1a1	GGCAACAGTCGCTTCACCTACAG	GAGGTCTTGGTGGTTTTGTATTCG
Spp1	CTGATGAACAGTATCCTGATGCCAC	GGGACTCCTTAGACTCACCGCT
Sparc	TTGGCGAGTTTGAGAAGGTATGC	AGGTGACCAGGACATTTTTGAGC
Wnt3a	GGAGTTTGCCGATGCCAGGGAG	ACCACCAGCAGGTCTTCACTTCACAG
β-catenin	TCGTGCTGGTGACAGGGAAGAC	GCAGTCCATAATGAAGGCGAACG
RUNX2	GGAATGATGAGAACTACTCCGCCG	GAAACTCTTGCCTCGTCCGCTC
β-actin	AGGTCATCACTATTGGCAACGAG	TTGGCATAGAGGTCTTTACGGAT

Acan, aggrecan; Col1a1, collagen type I α1 chain; Col10a1, collagen type X α1 chain; Col2a1, collagen type II α1 chain; RUNX2, RUNX family transcription factor 2; Sparc, secreted protein acidic and cysteine rich; Spp1, secreted phosphoprotein 1.

Technology, Inc.) and anti-histone H3 antibody (1:2,000; cat. no. 4499; Cell Signaling Technology, Inc.), diluted in antibody diluent according to the manufacturer's instructions, were then added for incubation overnight at 4˚C with gentle shaking. The membranes were washed with TBS with 0.1% Tween-20 and incubated with the appropriate horseradish peroxidase-conjugated secondary antibodies (1:4,000; cat. no. S0001 or S0002; Affinity Biosciences, Ltd.) at room temperature for 1 h. The proteins were then exposed and stained with ECL reagent. On the same membrane, different primary antibodies were incubated successively. Before changing the primary antibody, the previous round of primary/secondary antibodies was eluted with Stripping buffer (Beyotime Biotechnology). The target bands were analyzed using ImageJ software (1.54p; National Institutes of Health) for gray-value calculations.

Chromatin immunoprecipitation-PCR (ChIP-PCR). ChIP-PCR was used to observe the changes in H3K27me2 and H3K27me3 in the promoter region of Wnt3a, β-catenin and RUNX2 in the fx/wt normoxia group and the fx/fx normoxia group after 3 days of osteogenic induction. The ChIP assay was performed using the ChIP Assay Kit (cat. no. P2078; Beyotime Biotechnology) according to the manufacturer's instructions. The cells were treated with 1% formaldehyde to form covalent cross-links between intracellular DNA-bound proteins and DNA and the cross-linking reaction was quenched with 125 mM glycine. Cells were lysed with 1 mM PMSF in SDS Lysis Buffer (included in the ChIP Assay Kit) (200 μl/10^6 cells), and the genomic DNA was subsequently fragmented by sonication (20 kHz; 4 sec pulse; 8 sec interval; at a rate of 5 times per min for a total of 5 min in an ice-water bath) to obtain random fragments typically ranging between 200 and 1,000 bp. Specific antibodies against the target proteins were used, including anti-histone H3 (di methyl K27) (1:50; cat. no. 9728; Cell Signaling Technology, Inc.), anti-histone H3 (tri methyl K27) (1:50; cat. no. 9733; Cell Signaling Technology, Inc.) and IgG (cat. no. 2729; Cell Signaling Technology, Inc.). These antibody-chromatin complexes were subsequently captured with 60 μl Protein A+G Agarose beads (included in the ChIP Assay Kit) to enrich the DNA fragments bound by the target proteins. Subsequently, the instructions in the kit (cat. no. P2078; Beyotime Biotechnology) were followed to wash the precipitate. The wash procedure was performed sequentially with Low Salt Immune Complex Wash Buffer, High Salt Immune Complex Wash Buffer, LiCl Immune Complex Wash Buffer and TE Buffer. The cross-linking of proteins and DNA was relieved by centrifugation (1,000 x g; 1 min; 4˚C) and heating, and proteins were degraded using proteinase K. The enriched DNA fragments were purified using a DNA purification kit (cat. no. D0033; Beyotime Biotechnology). Purified DNA was used as a template for PCR amplification using PrimeSTAR® HS DNA Polymerase (Takara Bio, Inc.). The primer sequences are listed in Table II. The amplification reaction conditions were as follows: 30 cycles of 98˚C for 10 sec, 60˚C for 15 sec and 72˚C for 50 sec. The PCR products were separated by 1.5% agarose gel electrophoresis, stained with GelStain fluorescent nucleic acid dye (TransGen Biotech Co., Ltd.) and visualized using a fully automatic digital gel imaging analysis system (Tanon Science and Technology Co., Ltd.).

Table II. Nucleotide sequences of primers used for chromatin immunoprecipitation-PCR amplification.

Target gene	Primer sequence (5'-3')	Size, bp
Wnt3a		473
Forward	AGGGTCTTTTCTCTGGGCTACAA	
Reverse	ATCTCAACCTATGGGGGTCACAG	
β-catenin		657
Forward	TTGACAAGTGCCAATCGTGAAGG	
Reverse	AAAGTAGTCCCCGCCAGTCCG	
RUNX2		890
Forward	ACTGTCCACGCTGATGAAAGAAT	
Reverse	TGTCTCTTTACTTATGGGTGTTCCT	

RUNX2, RUNX family transcription factor 2.

Micro-CT analysis. Micro-CT was used to assess the bone structure and fracture healing (49). At 28 days post-fracture, the mice underwent *in vivo* micro-CT scanning and three-dimensional reconstruction to observe morphological changes at the fracture site. The mice were initially anesthetized in an induction chamber with 4% isoflurane delivered in air at a flow rate of 1 l/min via a gas anesthesia machine. Once anesthetized, the mouse was transferred to a nose cone for maintenance on 1.8% isoflurane in air at a flow rate of 0.8 l/min throughout the scanning procedure. The positions of the mouse and scanning chamber were carefully fixed, an appropriate scanning bed was selected, and imaging was performed, followed by three-dimensional reconstruction to obtain images for subsequent analysis.

For *ex vivo* scanning, the bone samples were placed in a small sample holder for scanning and three-dimensional reconstruction to collect data for subsequent analyses. On day 28 post-fracture, tibial specimens were collected and then fixed in 4% paraformaldehyde at 4˚C for 48 h. After fixation, the samples were wrapped in gauze and placed in a small *ex vivo* chamber for standard micro-CT scanning and three-dimensional reconstruction (parameters: tube voltage, 70 kV; tube current, 150 μA; reconstruction algorithm, Feldkamp-Davis-Kress; resolution, 1k x 1k). After reconstruction, the images were segmented and bone analysis was performed using Avatar3 software [2.0.12.0; PINGSENG Healthcare (Kunshan) Inc.]. The region of interest was defined as an area 1 mm above and below the fracture line. Quantitative analyses were performed to determine the trabecular bone volume fraction (BV/TV), trabecular bone surface area fraction (BS/TV), trabecular number (Tb.N) and trabecular thickness (Tb.Th).

Statistical analysis. Cluster-specific marker genes were identified using the Wilcoxon rank-sum test implemented in the FindAllMarkers function of the Seurat package, with an adjusted P-value <0.05 and $|avglog_2$ fold change (FC)$|>0.25$ as thresholds. Differentially expressed genes between groups were explored using the FindMarkers function with the built-in Wilcoxon rank-sum test, with an adjusted P-value <0.05 and $|avglog_2FC|>0.15$. The experimental data were obtained from at least three independent replicates. Statistical analyses of all data were performed using GraphPad Prism (version 8.0.2; Dotmatics). Data were normally distributed. Comparisons between two groups were analyzed using a two-tailed, unpaired Student's t-test. For comparisons among multiple groups, one-way ANOVA was performed, followed by Tukey's post hoc test. Data are presented as the mean ± SD. P<0.05 was considered to indicate a statistically significant difference.

Results

Transcriptional landscape of callus tissue during mouse fracture healing. First, six fx/wt (WT) mouse fracture callus samples were analyzed, including three samples collected at 10 days post-fracture (WT1_10, WT2_10 and WT3_10) and three samples collected at 21 days post-fracture (WT1_21, WT2_21 and WT3_21). Following quality control and data filtering, 56,189 high-quality deeply sequenced cells were obtained and 25 distinct clusters were identified. Each cluster was defined by comparing its expression profile with that of known lineage markers or canonical gene signatures.

During cell annotation, dimensionality reduction and unbiased clustering were performed based on gene expression profiles and classical markers of the cells, resulting in the identification of 19 clusters (Fig. 1A). There were distinct differences in the UMAP plots between callus samples collected 10 and 21 days after fracture, indicating different cellular compositions at these stages (Fig. 1B). The present study focused particularly on six CH subpopulations: i) Proliferative CHs, characterized by high expression levels of Ucma, C1qtnf3, Cnmd, Itm2a and Scrg1; ii) pre-HTCs, marked by elevated levels of Cdkn1c, Hapln1, Ppa1, Pth1r and Snorc; iii) HTCs, expressing Col10a1, Cst3, Spp1, Ihh and Ddit4l; iv) CH-derived osteoprogenitors (CDOPs), distinguished by high expression levels of Mmp13, Spp1, osteomodulin (Omd), matrix Gla protein (Mgp) and MAF bZIP transcription factor B (Mafb); v) osteoblasts, identified by the expression of Bglap, Bglap2, Ifitm5, Ibsp and Col1a1; and vi) osteoclasts, which specifically expressed Acp5, Ctsk, Ckb, S100a4 and Mmp9 (Fig. 1C).

Proportion plots were generated for each cell type (Fig. 1D). At 10 days post-fracture, CHs in the tissue were in a rapid proliferative phase, with pre-HTCs, HTCs and CDOPs constituting a larger proportion. Osteoblasts were already present but at relatively low levels. By day 21, the proportion of CHs had markedly decreased, indicating that hypertrophy and transdifferentiation were near completion, whereas the numbers of endothelial cells and osteoclasts had increased, accelerating vascular invasion and cartilage matrix degradation.

The volcano plot demonstrated that a special CDOP subset was distinguished by the co-expression of a specific set of marker genes, including Mmp13, Spp1, Mgp, Omd and Mafb (Fig. 1E). The expression profiles of key representative genes during CH transdifferentiation, including Col2a1, Sox9, Col10a1, Mmp13, RUNX2, Spp1, Sp7 (Osx) and Col1a1, were examined and visualized using UMAP and violin plots (Fig. 1F and G). Dot plot analysis revealed that CDOPs co-expressed Col2a1 and Col1a1, and lacked HTC marker Col10a1, suggesting active matrix mineralization, remodeling and proliferation (Fig. 1H) (35).

Systematic functional analysis of endochondral ossification-related differentially expressed gene clusters in CDOPs revealed that the core differential genes, according to GO functional annotation, were significantly enriched in key biological processes such as 'protein binding' (molecular function), 'chondrocyte differentiation' (biological process) and 'skeletal system development' (cellular component). Notably, these genes were highly associated with 'ossification' and 'bone development' (Fig. 1I). KEGG pathway enrichment analysis further demonstrated that the differential genes were primarily involved in the 'FoxO signaling pathway', 'TGF-β signaling pathway', 'MAPK signaling pathway', 'ECM-receptor interaction' and 'PI3K-Akt signaling pathway' (Fig. 1J). These pathways collectively mediate the establishment of the osteogenic microenvironment through the coordinated regulation of cell cycle progression, proliferative and differentiation dynamics, migratory and adhesive behaviors, and matrix remodeling capacity. The significant enrichment of 'signaling pathways regulating pluripotency of stem cells' (Fig. 1J) suggested that CDOPs may possess the

SPANDIDOS PUBLICATIONS

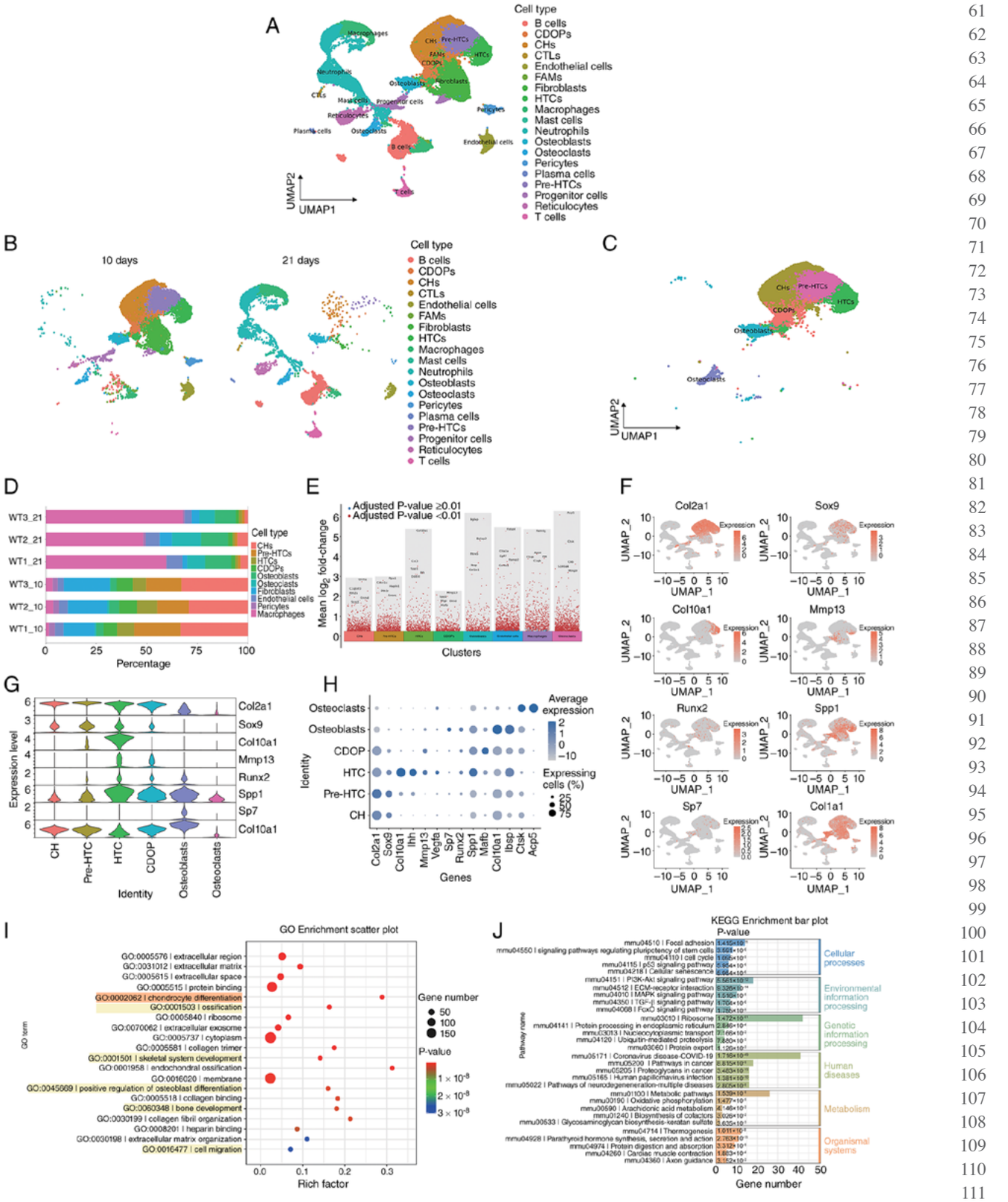

Figure 1. Transcriptional landscape of callus tissue during mouse fracture healing. (A) UMAP plot displaying 19 major cell types identified in the callus tissue. (B) UMAP plots of tissue samples collected from WT mice at 10 and 21 days post-fracture. (C) UMAP plots showing six subpopulations of CH-osteoblast lineage cells. (D) Proportion plots of the cell types of interest for each tissue sample. (E) Volcano plots of differentially expressed genes for the subpopulations of interest. (F) UMAP plots of characteristic marker genes for CH-osteoblast subpopulations. Deeper colors indicate higher expression levels of the feature gene in specific cell populations. (G) Expression profiles of the key representative genes in each subpopulation during CH transdifferentiation. (H) Dot plot showing the expression of 14 characteristic marker genes across the six subpopulations. Dot size represents the proportion of cells expressing a particular marker, whereas the color gradient indicates the average expression level of the marker. (I) Bubble plot of GO functional enrichment analysis of genes in cluster 5 (CDOP). (J) Bar plot of KEGG pathway enrichment analysis of genes in cluster 5 (CDOP). For each timepoint, callus tissues were harvested from three independent mice (n=3 biologically independent animals per timepoint). CDOP, chondrocyte-derived osteoprogenitor; CH, chondrocyte; CTL, cytotoxic T lymphocyte; FAM, fibroblastic reticular cell-associated macrophage; GO, Gene Ontology; HTC, hypertrophic chondrocyte; KEGG, Kyoto Encyclopedia of Genes and Genomes; UMAP, uniform manifold approximation and projection; WT, wild-type.

potential for mesenchymal stem cell differentiation toward the osteogenic lineage.

Differentiation of CDOPs into osteoblasts during endochondral ossification is regulated by the oxygen environment. Based on trajectory inference analysis of single-cell transcriptomic data, the present study utilized the Monocle3 algorithm to perform pseudo-time modeling of six relevant cell subpopulations involved in the transdifferentiation process of CHs. UMAP nonlinear dimensionality reduction (Fig. 2A) was used to construct a continuum of cellular states, followed by integration with RNA velocity to resolve the topological structure of the cell differentiation trajectories. Using CHs as the starting point of the trajectory (pseudotime t=0), the results revealed a pronounced bifurcation in cell fate with notable bidirectional heterogeneity: The primary branch (branch 1) culminated in osteoblasts as the terminally differentiated state, while the secondary branch (branch 2) terminated in HTCs. Notably, osteoblasts were strictly localized to the terminal region of branch 1 along the pseudotime axis, with no significant temporal overlap in transcriptomic features with intermediate cell states, such as the CDOP subpopulation, suggesting that this subpopulation may undergo a rapid terminal differentiation program. By contrast, HTCs and CDOPs exhibited partially overlapping segments along the pseudo-time axis, indicating that they may share transitional regulatory networks. Further analysis examined the temporal changes in the expression of characteristic genes at various time points and across different cell subpopulations (Fig. 2B and C). Pseudotime analysis showed that 1700025G04Rik was highly expressed during the early stages of CH transdifferentiation, suggesting its potential role in driving the differentiation process. Collagen type III α1 chain (Col3a1) is primarily distributed in blood vessels, marking vascular ingrowth during differentiation, and together with Col1a1, helps maintain tissue tensile strength (50). Collagen type V α2 chain (Col5a2) serves a regulatory role in the assembly of Col1a1, thereby influencing collagen fiber diameter and organization of the extracellular matrix (51). Serpin family E member 2 (Serpine2) inhibits plasmin and thrombin, thereby regulating ECM remodeling, axon guidance and synaptic plasticity (52). Myosin IB (Myo1b), an unconventional myosin, modulates the interplay between the cell membrane and the cytoskeleton through its association with actin. Myo1b participates in vesicle trafficking and cell migration, and serves a crucial role in the regulation of diverse cellular functions, including cell proliferation and apoptosis (53). During the transdifferentiation process, Col5a2, Myo1b and Serpine2 expression progressively increased, peaking at the terminal stage, whereas Col3a1 expression remained stable during the CH phase and was gradually downregulated upon osteoblast commitment. Taken together, these findings suggested that CDOPs are the precursor subpopulations of osteoblasts, whereas conventional HTCs maintain paracrine regulatory roles during endochondral ossification.

GO functional enrichment analysis of the top 100 differentially expressed genes (Fig. 2D) revealed the following: First, the core biological themes were skeletal development and remodeling, as evidenced by terms such as 'endochondral ossification', 'skeletal system development' and 'ossification'. There were also implicit connections, such as strong enrichment of 'ECM proteoglycans' and the 'PID INTEGRIN1 PATHWAY', indicating that dynamic remodeling of the extracellular matrix was a driving force in bone formation. Second, crosstalk between signaling pathways was apparent: The enrichment of the 'PID INTEGRIN1 PATHWAY' along with the 'response to mechanical stimulus' suggested that integrins may regulate CH differentiation by sensing mechanical signals (such as the piezoelectric effect in bones). The 'PID SYNDECAN 4 PATHWAY' and its association with ECM proteoglycans may mediate cell matrix adhesion and coordinate with growth factors (such as cell adhesion molecule and BMP). Third, enrichment of 'ECM proteoglycans' and 'keratan sulfate biosynthesis' underscored the critical role of glycosaminoglycan modifications in establishing and maintaining a CH-to-osteoblast transition microenvironment. The term 'negative regulation of molecular function' likely reflected the precise control of matrix degradation by protease inhibitors, such as Serpine2. Fourth, microenvironmental homeostasis mechanisms were highlighted by terms such as 'hemostasis' and 'blood vessel development', indicating the coupled roles of angiogenesis, coagulation factors and the oxygen microenvironment in bone repair processes. Enrichment of the 'apoptotic signaling pathway' and 'positive regulation of execution phase of apoptosis' likely reflected the contribution of programmed death of HTCs to the progression of ossification.

Safranin O/Fast Green staining of callus tissues harvested from the fracture sites at 10 and 21 days post-fracture was performed (Fig. 2E). On day 10, the robust formation of cartilaginous calluses was observed in all groups. The extracellular matrix of HTCs, rich in proteoglycans, was intensely stained red by Safranin O, indicating that the cartilage tissue constituted the majority of the callus at this stage, with only a small proportion of gray-blue-stained osteogenic areas present. A marked increase in the number and proportion of tdTomato^{+}/OCN^{+} double-positive cells indicative of CH-derived osteoblasts was evident from the immunofluorescence images comparing fracture calli at day 10 and day 21 post-fracture (Fig. 2E).

Oxygen availability facilitates the osteogenic differentiation of CHs via KDM6A. Given that KDM6A acts as an oxygen sensor to regulate cellular differentiation (22), the present study investigated how CH-to-osteoblast differentiation during endochondral ossification is altered under different oxygen levels. CHs derived from fx/wt and fx/fx mice were subjected to transdifferentiation induction. After 7 days of induction, Alcian blue staining (Fig. 3A and B) revealed that the fx/wt-normoxic group exhibited a significantly lower amount of acidic mucopolysaccharides than the fx/wt-hypoxic group ($P<0.05$), while the fx/fx-normoxic group showed a significant increase in acidic mucopolysaccharides compared with the fx/wt-normoxic group ($P<0.01$). ALP staining (Fig. 3C and D) demonstrated that the number of ALP-positive cells was markedly higher in the fx/wt-normoxic group than in the fx/wt-hypoxic group ($P<0.001$), whereas the number of ALP-positive cells in the fx/fx-normoxic group was significantly lower than that in the fx/wt-normoxic group ($P<0.001$). Alizarin red staining (Fig. 3E and F) indicated an increased number of mineralized nodules in the fx/wt-normoxic group compared with the fx/wt-hypoxic group ($P<0.05$), whereas the

SPANDIDOS PUBLICATIONS

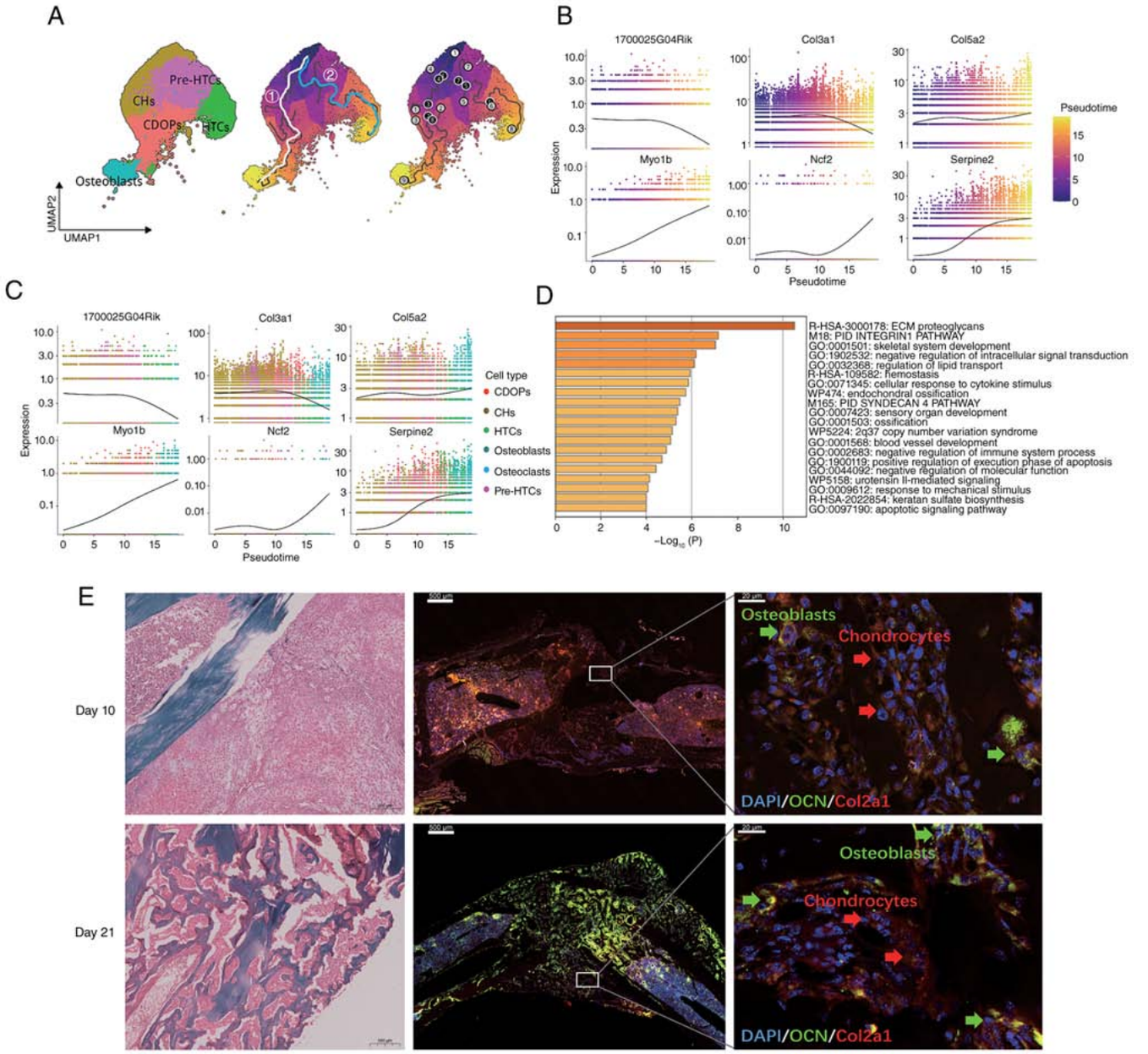

Figure 2. Differentiation of CDOPs into osteoblasts during endochondral ossification is regulated by the oxygen environment. (A) UMAP plot showing the distribution of cell subpopulations, with a pseudo-time trajectory from CHs to osteoblasts/HTCs that included both fates 1 and 2. The trajectory plot shows the underlying graph structure as black lines. The white line indicates fate 1, representing the transdifferentiation path from CHs through the transitional CDOP state to osteoblasts. The blue line indicates fate 2, depicting the differentiation path from CHs through pre-HTCs to HTCs. White circles represent roots, gray circles indicate terminal fates (leaves) and black circles denote the branch points from which cells can diverge toward multiple fates. (B) Pseudotime expression plots for the top six genes, illustrating their dynamic changes along the differentiation trajectory. (C) Expression profiles of the top six genes across the different cell subpopulations. (D) Bar plot of GO functional enrichment for the top 100 genes, colored by P-value. (E) Representative Safranin O/Fast Green staining images of mouse tibial fracture callus at 10 and 21 days post-fracture (scale bar, 200 μm), and immunofluorescence staining images showing OCN$^+$ and Col2a1-tdTomato$^+$ cells (scale bars, 500 and 20 μm). For each timepoint, callus tissues were harvested from three independent mice (n=3 biologically independent animals per timepoint). OCN, osteocalcin; CDOP, chondrocyte-derived osteoprogenitor; CH, chondrocyte; Col2a1, collagen type II α1 chain; Col3a1, collagen type III α1 chain; Col5a2, collagen type V α2 chain; ECM, extracellular matrix; GO, Gene Ontology; HTC, hypertrophic chondrocyte; Myo1b, myosin IB; Ncf2, neutrophil cytosolic factor 2; PID, Pathway Interaction Database; Serpine2, serpin family E member 2; UMAP, uniform manifold approximation and projection.

fx/fx-normoxic group had fewer mineralized nodules than the fx/wt-normoxic group (P<0.05).

qPCR analysis of CH marker gene expression 3 days after induction (Fig. 3G) showed that the mRNA levels of Col10a1, Acan and Col2a1 were reduced in the fx/wt-normoxic group compared with the fx/wt-hypoxic group (P<0.05, P<0.01 and P<0.0001, respectively). By contrast, fx/fx-normoxic mice exhibited increased expression of all three genes compared with fx/wt-normoxic mice (P<0.05), with a particularly significant upregulation of Col2a1 and Acan (P<0.0001). Furthermore, analysis of the relative mRNA levels of osteogenic differentiation-related genes (Fig. 3H) revealed that Col1a1, Spp1 and Sparc were significantly upregulated in the fx/wt-normoxic group compared with the fx/wt-hypoxic group

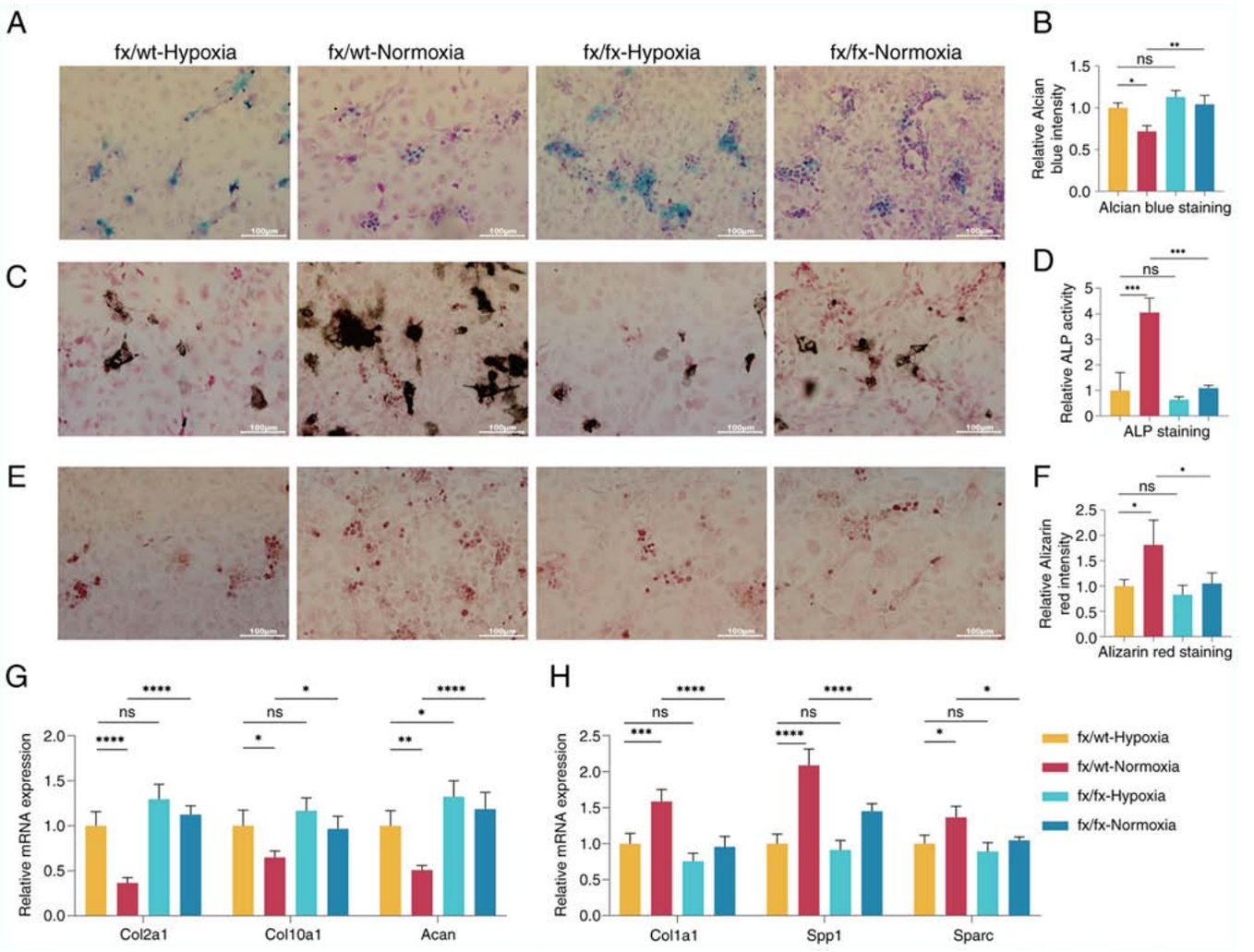

Figure 3. Oxygen availability facilitates the osteogenic differentiation of CHs via lysine demethylase 6A. (A) Alcian blue staining of cells from each group after 7 days of induction (scale bar, 100 μm). (B) Quantitative analysis of Alcian blue staining in each group. (C) ALP staining of cells from each group after 7 days of induction (scale bar, 100 μm). (D) Quantitative analysis of ALP staining in each group. (E) Alizarin red staining of cells from each group after 7 days of induction (scale bar, 100 μm). (F) Quantitative analysis of Alizarin Red staining in each group. (G) Relative mRNA expression levels of CH marker genes in each group 3 days after induction. (H) Relative mRNA expression levels of osteogenic differentiation-related genes in each group 3 days after induction. n=3, data derived from three independent experiments. P-values were calculated using one-way ANOVA followed by Tukey's post hoc test. The values are presented as the mean ± SD. *P<0.05, **P<0.01, ***P<0.001 and ****P<0.0001. Acan, aggrecan; ALP, alkaline phosphatase; CH, chondrocyte; Col1a1, collagen type I α1 chain; Col10a1, collagen type X α1 chain; Col2a1, collagen type II α1 chain; fx, Kdm6a conditional knockout mice; IntDen, integrated density; ns, not significant; Sparc, secreted protein acidic and cysteine rich; Spp1, secreted phosphoprotein 1; wt, wild-type.

(P<0.001, P<0.0001 and P<0.05, respectively). However, the expression levels of all three genes were markedly reduced in the fx/fx-normoxic group compared with the fx/wt-normoxic group (P<0.0001, P<0.0001 and P<0.05, respectively).

KDM6A promotes the differentiation of CHs into CDOPs by activating the Wnt signaling pathway. scRNA-seq was also performed on chondral callus cell samples from fx/wt (WT) and fx/fx mice (FX), 10 days post-fracture. The analysis focused on CHs, pre-HTCs, HTCs, CDOPs and osteoblasts (Fig. 4A). Violin plots of gene expression (Fig. 4B) revealed that the mean expression levels of Col2a1 in the WT group were lower than those in the FX group, whereas Col10a1, RUNX2 and Col1a1 were more highly expressed in the WT group than in the FX group. The expression levels of Acan and Bglap were similar in the two groups. The present study specifically focused on the CDOP subpopulation. The volcano plot of differentially expressed genes showed that osteogenic genes, including Col1a1, Sp7, RUNX2 and Spp1, were significantly upregulated in CDOPs of the WT group compared with those of the FX group (Fig. 4C). GO analysis indicated that the upregulated genes were enriched in biological processes, such as 'cell adhesion', 'chondrocyte differentiation', 'skeletal system development', 'endochondral ossification' and 'osteoblast differentiation'. Pathway analysis revealed that the 'Wnt signaling pathway' was the most prominent osteogenic pathway enriched in our dataset (Fig. 4D and E). GSEA (Fig. 4F) indicated that the 'Wnt signaling pathway' was significantly enriched in the WT group (enrichment score, 0.276; P=0.0063; false discovery rate, 0), suggesting that global Wnt pathway activity was higher in WT cells.

CellChat analysis identified intercellular communication among the 16 clusters detected in callus samples on day 10 post fracture, revealing extensive molecular interactions

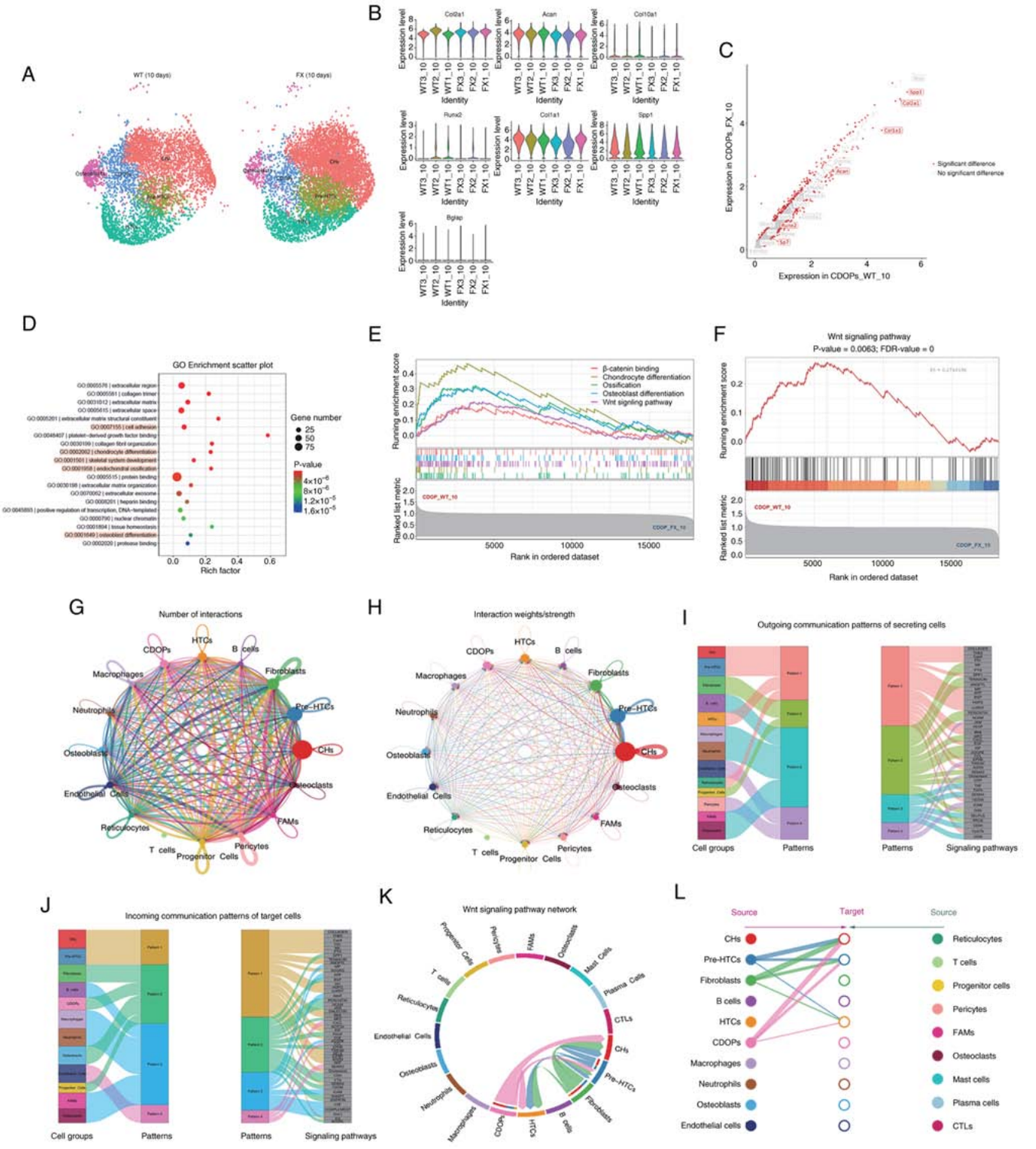

Figure 4. Lysine demethylase 6A promotes the differentiation of CHs into CDOPs by activating the Wnt signaling pathway. (A) UMAP visualization of CH and osteoblast subpopulations in WT and FX groups. (B) Violin plots showing the average expression levels of marker genes across six samples. (C) Volcano plot depicting upregulated genes in CDOPs between the WT and FX groups. (D) Bubble plot of GO functional enrichment analysis of upregulated genes in CDOPs. (E) Line graph of gene set enrichment analysis enrichment scores for upregulated genes in CDOPs based on the GO database. (F) Line graph of enrichment scores from the Kyoto Encyclopedia of Genes and Genomes pathway analysis showing upregulation of the Wnt pathway in CDOPs. (G) Network plot illustrating the number of interactions between any two cell groups. (H) Network plot displaying the interaction strength between any two cell groups. (I) Visualization of outgoing communication patterns of cell populations. (J) Visualization of incoming communication patterns of cell populations, with Sankey diagrams showing relationships between cell clusters and patterns, as well as between pathways and patterns. (K) Chord diagram of Wnt signaling pathway interactions among CH subpopulations. (L) Hierarchical plot of Wnt signaling pathway interactions among CH subpopulations. Source (left) and target (right) cell populations are represented by colored circles. Connecting lines indicate inferred Wnt ligand-receptor interactions, with the line color corresponding to the source cell type and the line thickness proportional to the interaction probability/strength. The plot highlights CDOPs as a prominent source of Wnt signals within the chondro-osteogenic lineage, with CHs also contributing as a target. For each timepoint, callus tissues were harvested from three independent mice (n=3 biologically independent animals per timepoint). CDOP, chondrocyte-derived osteoprogenitor; CH, chondrocyte; CTL, cytotoxic T lymphocyte; ES, enrichment score; FAM, fibroblastic reticular cell-associated macrophage; FDR, false discovery rate; FX, Kdm6a conditional knockout mice; GO, Gene Ontology; HTC, hypertrophic chondrocyte; UMAP, uniform manifold approximation and projection; WT, wild-type.

(Fig. 4G and H). Sankey plots showed how 13 sender cell populations (acting as signaling sources) coordinated with one another and with specific signaling pathways to drive communication, and how 12 receiver cell populations (acting as targets) coordinated to respond to incoming signals (Fig. 4I and J). Notably, CHs and CDOPs exhibited the highest frequency of intercellular interactions via the Wnt signaling pathway (Fig. 4K). Furthermore, the hierarchical plot (Fig. 4L) delineated the sending and receiving roles of different CH subsets within the Wnt signaling network, highlighting CDOPs as key signaling hubs.

KDM6A deficiency inhibits endochondral ossification under normoxic conditions by suppressing the Wnt/β-catenin pathway through enhanced histone H3K27 methylation. Western blot analysis was performed to assess the histone methylation levels in CHs from fx/wt-normoxic and fx/fx-normoxic cells during transdifferentiation. H3K27me2 and H3K27me3 levels were normalized to those of total histone H3 (loading control) to quantify relative changes in these histone modifications independently of total protein variation. As shown in Fig. 5A, the expression levels of H3K27me2 and H3K27me3 proteins were significantly higher in the fx/fx-normoxic group than in the fx/wt-normoxic group ($P<0.001$). ChIP-PCR (Fig. 5B) showed that enrichment of H3K27me2 and H3K27me3 at the Wnt3a promoter region was markedly increased in the fx/fx normoxic group compared with the fx/wt-normoxic group. H3K27me3 enrichment at the RUNX2 promoter was also higher in the fx/fx-normoxic group than in the fx/wt-normoxic group. Additionally, the protein expression levels of Wnt3a, β-catenin and RUNX2 (Fig. 5C and D) were reduced in the fx/fx-hypoxic group compared with the fx/wt-hypoxic group ($P<0.05$). In addition, the fx/wt-normoxic group exhibited significantly higher expression levels of β-catenin and RUNX2 compared with the fx/wt-hypoxic group ($P<0.001$), while Wnt3a expression was also increased ($P<0.01$). By contrast, the expression levels of all three proteins were significantly decreased in fx/fx-normoxic mice compared with fx/wt-normoxic mice ($P<0.001$). Differences in the mRNA expression levels of Wnt3a, β-catenin and RUNX2 (Fig. 5E) among the groups were in accordance with their respective protein expression patterns.

KDM6A deletion inhibits the transdifferentiation of CHs within the cartilage callus and delays fracture healing in mice. The present study subsequently investigated the impact of KDM6A deletion on fracture healing in mice. H&E staining (Fig. 6A) showed that at 10 days post-fracture, both fx/wt and fx/fx mice exhibited calluses comprising a small amount of fibrous tissue and a large amount of cartilage tissue, with woven bone already formed in both groups. Notably, the fx/wt group displayed a greater amount of woven bone than the fx/fx group. By day 28 post-fracture, the bone entered the remodeling phase; the woven bone in the fx/fx group appeared loose and irregular, whereas the fracture ends in the fx/wt group were smoother. In the fx/wt group, the woven bone transformed into lamellar bone, with a relatively continuous lamellar bone observed, suggesting a better degree of healing than in the fx/fx group.

At 28 days post-fracture, *in vivo* micro-CT scanning and three-dimensional reconstruction (Fig. 6B) were performed to assess the morphology of the fracture ends. In the fx/wt group, a cortical bone bridge was formed, with no obvious peripheral callus observed, and partial recanalization of the medullary cavity was evident. By contrast, in the fx/fx group, a bone bridge was present, but the peripheral callus was not completely resorbed. *Ex vivo* micro-CT standard scanning and three-dimensional reconstruction (Fig. 6B) were performed on the harvested mouse tibiae to assess bone microarchitecture at the fracture ends. Three-dimensional views from the lateral, medial and dorsal aspects of the tibia, as well as two-dimensional sagittal and coronal sections, revealed that both groups exhibited bony union at the fracture site, with varying degrees of endosteal and periosteal callus resorption. Calli in the remodeling phase were observed in the outer cortex. On two-dimensional sagittal and transverse sections, irregular block-like intramedullary calluses were visible at the fracture ends, which were more pronounced in the fx/fx group. Quantitative analyses were conducted for BV/TV, BS/TV, Tb.N and Tb.Th within 1 mm of and below the fracture line (Fig. 6C). In the fx/fx group, both BV/TV and BS/TV were significantly higher than those in the fx/wt group ($P<0.01$), whereas Tb.N was also higher in the fx/fx group ($P<0.05$); no significant difference in Tb.Th was observed ($P>0.05$).

Immunofluorescence staining for OCN at the fracture callus at 10 and 21 days (Fig. 6D) was performed to assess the proportion of CH-to-osteoblast transdifferentiation. KDM6A deletion resulted in a significant reduction in transdifferentiation efficiency on day 10 (Fig. 6E; $P<0.01$) and a further decrease by day 21 (Fig. 6G; $P<0.001$). Safranin O/Fast Green staining (Fig. 6F) on day 10 post-fracture revealed active cartilage callus formation in both groups, with HTC-rich matrix stained bright red (proteoglycan content) and cartilage predominating in the callus, while a few gray-blue-stained osteogenic regions were visible. The fx/wt group had a greater osteogenic area than the fx/fx group, and the latter had fewer gray-blue regions than the former. At 21 days post-fracture, the red-stained cartilage area in the fx/wt group was decreased, indicating active ossification, and the gray-blue osteogenic area was increased; the red cartilage alternated with the loose gray-blue woven bone. In the fx/fx group, abundant red cartilage regions persisted, and the gray-blue woven bone was sparser, indicating a lower degree of ossification compared with the fx/wt group.

Discussion

The present study provided compelling evidence for a novel regulatory axis in fracture healing, in which the oxygen-sensing histone demethylase KDM6A orchestrated CH-to-osteoblast transdifferentiation through epigenetic activation of the Wnt/β-catenin pathway. Using an integrated approach combining scRNA-seq, genetic lineage tracing and conditional gene knockout, the cellular dynamics and molecular mechanisms underlying this critical bone repair process were delineated.

Single-cell transcriptomic analysis of the fracture calli at different time points (days 10 and 21) revealed a previously unknown complexity in CH differentiation trajectories during endochondral ossification. A distinct population of CDOPs that represent a transitional state between HTCs and mature osteoblasts was identified. These CDOPs co-expressed both

SPANDIDOS PUBLICATIONS

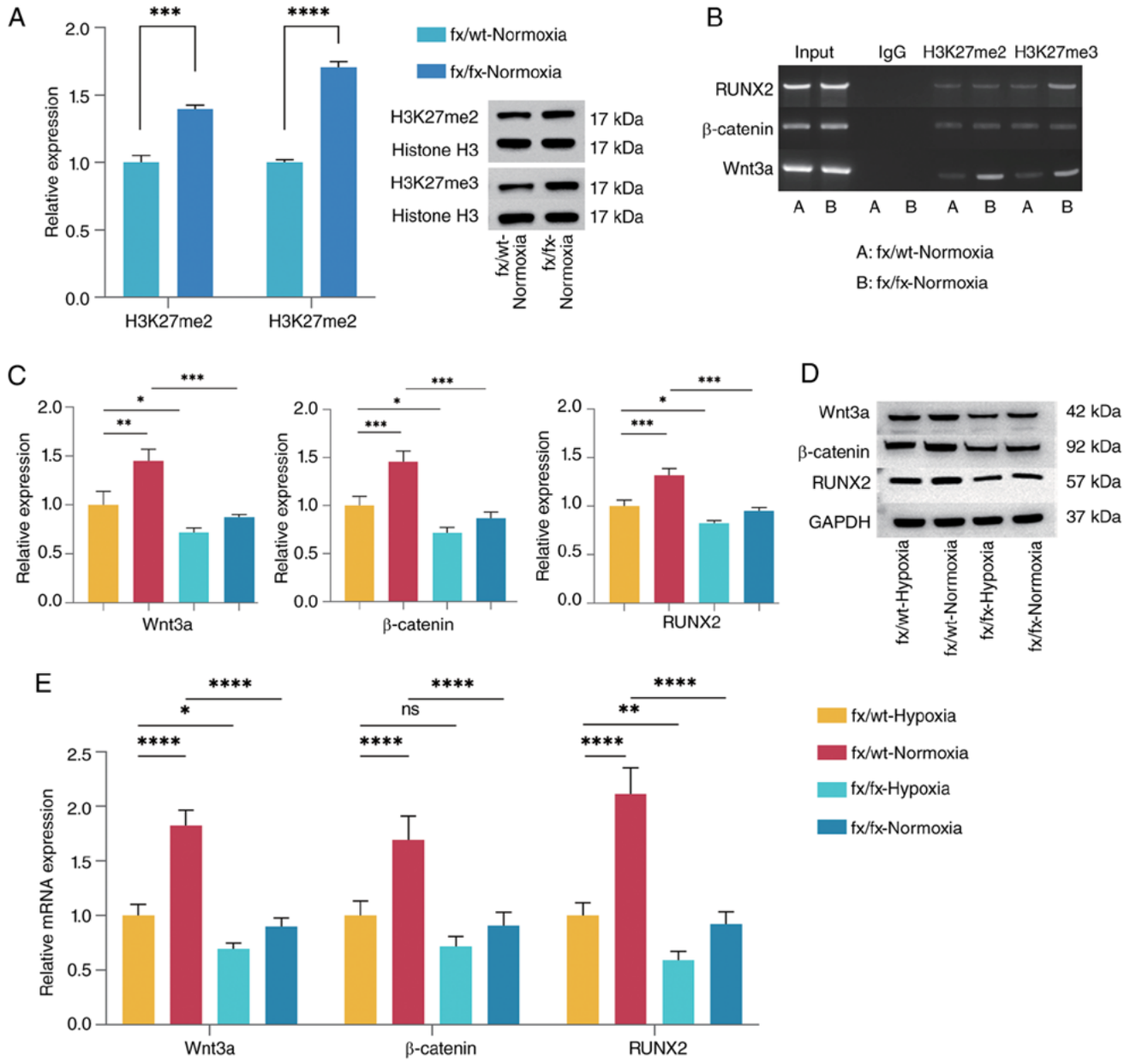

Figure 5. Lysine demethylase 6A deficiency inhibits endochondral ossification under normoxic conditions by suppressing the Wnt/β-catenin pathway through enhanced histone H3K27 methylation. (A) Densitometric analysis of H3K27me2 and H3K27me3 protein bands. Representative western blot bands of H3K27me2 and H3K27me3 are shown. Statistical analysis was performed using unpaired t-tests. The values are presented as the mean ± SD, ***P<0.001, ****P<0.0001. (B) Gel electrophoresis of chromatin immunoprecipitation-PCR showing differences in H3K27me2 and H3K27me3 enrichment at the Wnt3a, β-catenin and RUNX2 promoter regions between the two groups. (C) Densitometric analysis of the Wnt3a, β-catenin and RUNX2 protein bands. P-values were calculated using one-way ANOVA followed by Tukey's post hoc test. (D) Representative protein bands for Wnt3a, β-catenin and RUNX2. (E) Relative mRNA expression levels of Wnt3a, β-catenin and RUNX2 in each group after 3 days of induction. n=3, data derived from three independent experiments. P-values were calculated using one-way ANOVA followed by Tukey's post hoc test. The values are presented as the mean ± SD. *P<0.05, **P<0.01, ***P<0.001, ****P<0.0001. fx, Kdm6a conditional knockout mice; H3K27me2, histone H3 lysine 27 dimethylation; H3K27me3, histone H3 lysine 27 trimethylation; RUNX2, Runt-related transcription factor 2; wt, wild-type.

chondrogenic (Col2a1) and osteogenic (Col1a1) markers, while exhibiting elevated expression of matrix remodeling genes, including Mmp13 and Spp1. This unique gene expression signature suggested that CDOPs serve an active role in modifying the extracellular environment to facilitate the transition from cartilage to bone. Pseudotime trajectory analysis further supported the existence of a direct differentiation pathway from CHs to osteoblasts through this CDOP intermediate, challenging the traditional view that HTCs primarily undergo apoptosis during endochondral ossification (9-12).

GO enrichment analysis of genes differentially expressed along the transdifferentiation trajectory provided crucial insights into the biological processes regulated by KDM6A. The significant enrichment of terms including 'skeletal system development', 'endochondral ossification' and 'ossification' directly links the identified gene set to bone formation processes. Particularly noteworthy was the concurrent enrichment of 'ECM proteoglycans' and 'PID INTEGRIN1 PATHWAY', indicating that KDM6A promoted a transcriptional program conducive to extensive extracellular matrix remodeling. This

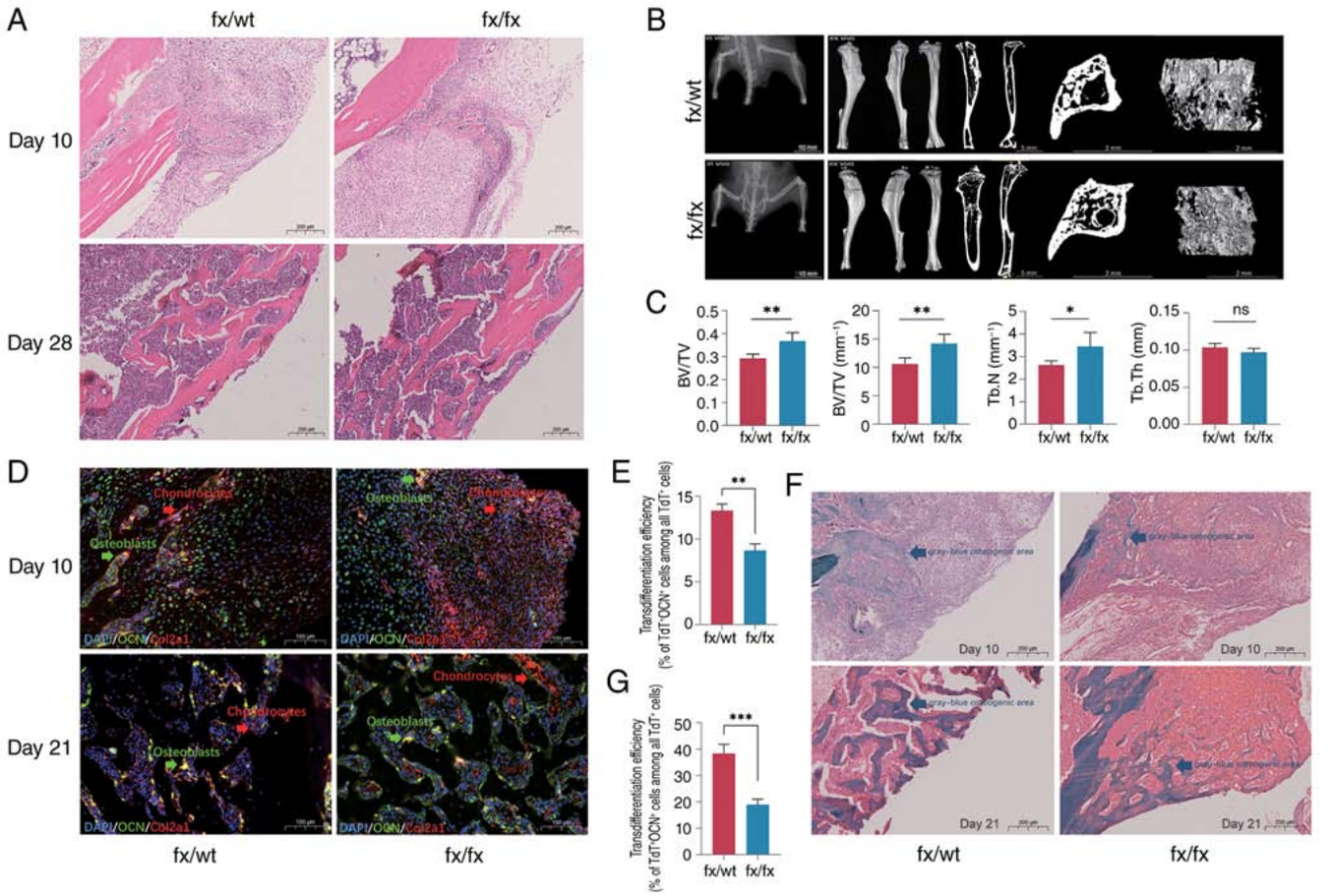

Figure 6. Lysine demethylase 6A deletion inhibits the transdifferentiation of CHs within the cartilage callus and delays fracture healing in mice. (A) Representative H&E staining of the fracture callus from each group at 10 and 28 days post-surgery (scale bar, 200 μm). (B) Micro-CT scans and three-dimensional reconstruction images at 28 days post-fracture (scale bar, 10 mm) showing lateral, medial and dorsal views, trabecular bone within 1 mm above and below the fracture site, and two-dimensional sagittal, coronal and transverse sections (scale bars, 5 and 2 mm). (C) Statistical analyses of BV/TV, BS/TV, Tb.N and Tb.Th. n=6; six samples in each group were independently derived from 6 separate mice. Statistical analysis was performed using unpaired t-tests. The values are presented as the mean ± SD. *P<0.05, **P<0.01. (D) OCN was marked with green fluorescence, CHs marked with tdTomato have inherent red fluorescence and the overlapping part in yellow indicates osteoblasts derived from CHs. Representative fluorescence images showing OCN^{+} and Col2a1 tdTomato^{+} cells (scale bar, 100 μm). (E) Quantification of transdifferentiation rates on day 10 post-fracture. n=3, three samples in each group were independently derived from 3 separate mice. Statistical analysis was performed using unpaired t-tests. The values are presented as the mean ± SD. **P<0.01. (F) Representative Safranin O/Fast Green staining of the fracture callus from each group at 10 and 21 days post-surgery (scale bar, 200 μm). (G) Quantification of transdifferentiation rates at day 21 post-fracture. For each timepoint, callus tissues were harvested from three independent mice (n=3 biologically independent animals per timepoint). Statistical analysis was performed using unpaired t-tests. The values are presented as the mean ± SD. ***P<0.001. OCN, osteocalcin; BS/TV, trabecular bone surface area fraction; BV/TV, trabecular bone volume fraction; CHs, chondrocytes; Col2a1, collagen type II α1 chain; fx, Kdm6a conditional knockout mice; ns, not significant; Tb.N, trabecular number; Tb.Th, trabecular thickness; TdT, tdTomato; wt, wild-type.

finding is consistent with the recognized importance of matrix remodeling in endochondral ossification (7), and suggests that KDM6A-mediated epigenetic regulation coordinates both cell fate determination and microenvironment modification. The co-enrichment of 'response to mechanical stimulus' with integrin signaling pathways further implies that KDM6A may help integrate biophysical cues with biochemical signals during fracture healing, representing a sophisticated mechanism for regulating bone repair in response to complex environmental signals.

To investigate the regulatory role of the oxygen microenvironment in endochondral ossification, an *in vitro* CH transdifferentiation model was established, and the effect of the oxygen environment on CH transdifferentiation was investigated by changing the oxygen concentration in the culture. Mice with cartilage-specific deletion of KDM6A were generated to explore the role of KDM6A in this process. CHs cultured under normoxic conditions exhibited greater osteogenic differentiation than those cultured under hypoxic conditions. The enhanced expression of osteogenesis-related marker genes (Col1a1, Spp1 and Sparc) and key Wnt/β-catenin pathway components (Wnt3a, β-catenin and RUNX2) under normoxic conditions promoted CH-to-osteoblast transdifferentiation. Conversely, the loss of KDM6A abrogated this pro-osteogenic effect of normoxia, resulting in a significant reduction in the expression of these molecules and a consequent impairment of osteogenic differentiation, indicating the importance of KDM6A in oxygen-mediated chondrogenic and osteogenic transdifferentiation. Single-cell sequencing results indicated that the influence of KDM6A was primarily exerted during the early and middle stages of transdifferentiation, specifically from CHs to the CDOP stage. Furthermore, KDM6A deficiency inhibited endochondral ossification under normoxic conditions by suppressing the Wnt/β-catenin pathway through enhanced histone H3K27 methylation. To further determine

SPANDIDOS PUBLICATIONS

the epigenetic target of KDM6A in the osteogenic differentiation of CHs, western blotting was performed to detect the levels of H3K27me2 and H3K27me3 in cells. The levels of H3K27me2 and H3K27me3 were significantly increased in KDM6A knockout cells, indicating that KDM6A serves a role in removing H3K27me2 and me3 during chondrogenic transdifferentiation. ChIP-PCR showed that KDM6A knockdown increased H3K27me2 and H3K27me3 levels in the Wnt3a promoter region, and H3K27me3 levels in the RUNX2 promoter region. Combined with the aforementioned experiments, we hypothesized that oxygen might remove histone H3K27me2 and me3 methylation in the Wnt3a promoter region and H3K27me3 methylation in the RUNX2 promoter region by activating KDM6A to relieve the transcriptional repression of Wnt3a and RUNX2. Consistent with the present findings, it has been widely reported that KDM6A activates the Wnt signaling pathway through H3K27 demethylation (54,55). A previous study has shown that KDM6A directly removes H3K27me3 modifications in the promoter regions of OCN and RUNX2 to initiate osteogenic differentiation in bone marrow mesenchymal stem cells (30). KDM6A activates RUNX2 and OSX by removing H3K27me3 and promotes MSCs differentiation into osteoblasts (31). KDM6A protein expression is increased during differentiation of MC3T3-E1 cells and primary osteoblasts. GSK-J1, a KDM6A inhibitor, increases H3K27me3 levels in the RUNX2 and osterix promoter regions in MC3T3-E1 cells. This inhibitor reduces the expression levels of RUNX2 and Osterix, and ALP activity, indicating that KDM6A serves an important role in osteoblast differentiation by regulating the expression of RUNX2 and Osterix (56). These findings are similar to the present results and confirm the important influence of KDM6A on cell differentiation at the epigenetic level. Previous studies have demonstrated that KDM6A is closely associated with embryonic development and genomic stability. KDM6A contains a JmjC domain and six tetratricopeptide repeat domains responsible for protein-protein interactions. Its activity is highly dependent on the oxygen concentration. However, KDM6A functions independently of classical HIF-1α (57,58). Unlike the HIF-1α pathway, which is mainly responsible for cell hypoxic adaptation and survival (16,17), KDM6A mediates a 'directive' pathway that directly determines cell fate (22). The two may act synergistically in hypoxic calli: HIF-1α provides the necessary metabolic basis and angiogenic conditions for regeneration, while the KDM6A-Wnt axis directly initiates the osteogenic transformation program.

Finally, the present study demonstrated that oxygen promoted the transdifferentiation of CHs into osteoblasts and facilitated fracture healing in mice by activating KDM6A, which upregulated the Wnt signaling pathway and RUNX2 expression. In KDM6A-deficient mice, woven bone formation was markedly reduced in the fractured callus on day 10 post-fracture. At 21 days after fracture, there were still more bright red cartilage areas in the callus of KDM6A-knockout mice, and the gray-blue woven bone was sparse. By day 28, during the bone remodeling phase, the callus in KDM6A-knockout mice retained a loose woven bone structure, and the healing process was delayed. Micro-CT analysis further revealed that following KDM6A deletion, irregular, bulky intramedullary calli remained at the fracture site and healing was slowed. Immunofluorescence staining of tibial tissue sections was performed using an anti-OCN antibody (green) to label osteoblasts. Since CHs were genetically labeled with tdTomato (red), cells exhibiting both green (OCN) and red (tdTomato) fluorescence were identified as CH-derived osteoblasts. The proportion of these double-positive cells relative to all tdTomato$^+$ cells was analyzed. KDM6A knockdown resulted in reduced transdifferentiation efficiency at both 10 and 21 days, visually demonstrating the effect of KDM6A on callus CH differentiation.

The core finding of the present study was that KDM6A was the key molecular switch that coordinated cell fate switching. Deletion of KDM6A inhibited the transcription of Wnt pathway genes by increasing H3K27me3 modification levels, thereby blocking the transformation trajectory from CHs to CDOPs and osteoblasts. Notably, cell communication analysis further suggested that KDM6A activity enhanced signal communication between various subsets of CHs. This suggested that KDM6A not only determines cell fate through a cell-autonomous mechanism but may also regulate the expression of cytokines to coordinate the behavior of cell populations in the endochondral osteogenic microenvironment at a broader scale and ensure the orderly progression of fracture repair.

The present study has some limitations. The fracture model was limited to a single tibial fracture in mice, and data from studies on other species and calluses in humans are lacking. In addition, to avoid the side effects of Tam on the reproductive system and hormone secretion in female mice (59), only male mice were used for the experiment. The generalizability and clinical relevance of the present findings to different biological settings, such as different species, sex and fracture sites, need to be further explored. Although the present study confirmed that KDM6A activated the Wnt/β-catenin pathway, it did not verify the broader upstream regulatory inputs or alternative downstream effector pathways of KDM6A beyond this axis. KDM6A may also serve a role in endochondral osteogenesis via a non-Wnt pathway. Future studies employing ChIP-seq could map the genome-wide binding sites of KDM6A, thereby clarifying its specific epigenetic regulation of Wnt target genes and potential effects on other pathways. The results of the cell experiments showed that a normoxic environment could promote the transdifferentiation of callus CHs into osteoblasts. Subsequent studies could include a hyperoxia group to further explore the effect of different oxygen concentrations on this process and screen the appropriate therapeutic concentration to promote transdifferentiation to provide a basis for clinical application. Oxygen-sensitive KDM6A was shown to be a therapeutic target for fracture healing. In the future, its spatiotemporally specific regulatory network can be further analyzed, and the combination of biomaterials, gene editing and precision medicine technology can promote the efficient transformation of this mechanism into clinical applications. Examples include local oxygen therapy at the fracture site (biomaterial delivery of oxygen) and targeting of KDM6A.

Novel KDM6A agonists could be developed as bone regeneration drugs. Their therapeutic potential may be enhanced through synergistic application with Wnt or BMP pathway modulators. Such a combination strategy could provide individualized treatment for patients whose stem cell osteogenic capacity is compromised by underlying diseases, ultimately

aiming to accelerate callus maturation and shorten the fracture healing cycle. In summary, the present study revealed that endochondral ossification during fracture healing was a highly coordinated, multi-step process in which CH-derived CDOPs differentiated into functional osteoblasts to complete bone tissue reconstruction. Oxygen accelerated fracture healing by activating KDM6A, which removed H3K27me2 and H3K27me3 methylation marks at the Wnt3a promoter and H3K27me3 at the RUNX2 promoter, thereby promoting CH differentiation into osteoblasts. These findings not only deepen the fundamental understanding of bone development and repair but also provide a theoretical basis for the development of epigenetics-based bone tissue engineering technologies and for optimizing clinical strategies for fracture treatment. Future research will focus on developing small-molecule compounds that specifically regulate KDM6A activity and explore their therapeutic potential in challenging bone injuries, such as osteoporotic fractures and nonunions.

Acknowledgements

Not applicable.

Funding

The present study was supported by the National Natural Science Foundation of China (grant no. 82205142), the Top Talent Support Program for Young and Middle-Aged People of the Wuxi Health Committee (grant no. HB 2023073), and the Postgraduate Research & Practice Innovation Program of Jiangsu Province (grant no. KYCX22_2062).

Availability of data and materials

The sequencing data generated in the present study may be found in the National Center for Biotechnology Information database under BioProject accession number PRJNA1267459 or at the following URL: https://www.ncbi.nlm.nih.gov/bioproject/PRJNA1267459. The other data generated in the present study may be requested from the corresponding author.

Authors' contributions

YR and HYu contributed to experiment design, data analysis and manuscript writing. HYi provided resources and contributed to designing and performing experiments. SL contributed to experiment design and reviewing the bioinformatics analysis. JW and ZS contributed to data analysis. XD, FB and TD contributed to data analysis, review and revision of the manuscript. GW and ZH contributed to conception and design, funding acquisition, and supervision. GW and ZH confirm the authenticity of all raw data. All authors have read and approved the final version of the manuscript.

Ethics approval and consent to participate

All animal protocols were approved by the Animal Care and Use Committee of Wuxi Affiliated Hospital of Nanjing University of Chinese Medicine (approval no. GZR2023032801; Wuxi, China).

Patient consent for publication

No applicable.

Competing interests

The authors declare that they have no competing interests.

References

1. GBD 2019 Fracture Collaborators: Global, regional, and national burden of bone fractures in 204 countries and territories, 1990-2019: A systematic analysis from the global burden of disease study. Lancet Healthy Longev 2: e580-e592, 2021.
2. Wildemann B, Ignatius A, Leung F, Taitsman LA, Smith RM, Pesántez R, Stoddart MJ, Richards RG and Jupiter JB: Non-union bone fractures. Nat Rev Dis Primers 7: 57, 2021.
3. Noorlander-Borgdorff MP, Şekercan A, Young-Afat DA, Bouman M, Botman M and Giannakópoulos GF: Nationwide study on open tibial fractures in the Netherlands: Incidence, demographics and level of hospital care. Injury 55: 111487, 2024.
4. Zhang S, Chen L, Zhang C, Gong C, He X, Zhong H, Liu C, Cao Z, Chen W, Lin N, *et al*: Osteoking exerts pro-osteogenic and anti-adipogenic effects in promoting bone fracture healing via EGF/EGFR/HDAC1/Wnt/β-catenin signaling. Int J Mol Med 55: 75, 2025.
5. Claes L, Recknagel S and Ignatius A: Fracture healing under healthy and inflammatory conditions. Nat Rev Rheumatol 8: 133-143, 2012.
6. Mathavan N, Singh A, Marques FC, Günther D, Kuhn GA, Wehrle E and Müller R: Spatial transcriptomics in bone mechanomics: Exploring the mechanoregulation of fracture healing in the era of spatial omics. Sci Adv 11: eadp8496, 2025.
7. Dennis SC, Berkland CJ, Bonewald LF and Detamore MS: Endochondral ossification for enhancing bone regeneration: Converging native extracellular matrix biomaterials and developmental engineering in vivo. Tissue Eng Part B Rev 21: 247-266, 2015.
8. Amizuka N, Hasegawa T, Oda K, Luiz de Freitas PH, Hoshi K, Li M and Ozawa H: Histology of epiphyseal cartilage calcification and endochondral ossification. Front Biosci (Elite Ed) 4: 2085-2100, 2012.
9. Aizawa T, Kokubun S and Tanaka Y: Apoptosis and proliferation of growth plate chondrocytes in rabbits. J Bone Joint Surg Br 79: 483-486, 1997.
10. Farnum CE and Wilsman NJ: Morphologic stages of the terminal hypertrophic chondrocyte of growth plate cartilage. Anat Rec 219: 221-232, 1987.
11. Farnum CE and Wilsman NJ: Condensation of hypertrophic chondrocytes at the chondro-osseous junction of growth plate cartilage in Yucatan swine: relationship to long bone growth. Am J Anat 186: 346-358, 1989.
12. Gibson G: Active role of chondrocyte apoptosis in endochondral ossification. Microsc Res Tech 43: 191-204, 1998.
13. Yang L, Tsang KY, Tang HC, Chan D and Cheah KSE: Hypertrophic chondrocytes can become osteoblasts and osteocytes in endochondral bone formation. Proc Natl Acad Sci USA 111: 12097-12102, 2014.
14. Giovannone D, Paul S, Schindler S, Arata C, Farmer DT, Patel P, Smeeton J and Crump JG: Programmed conversion of hypertrophic chondrocytes into osteoblasts and marrow adipocytes within zebrafish bones. Elife 8: e42736, 2019.
15. Im GI and Kim TK: Overcoming current dilemma in cartilage regeneration: Will direct conversion provide a breakthrough? Tissue Eng Regen Med 17: 829-834, 2020.
16. Stegen S, Laperre K, Eelen G, Rinaldi G, Fraisl P, Torrekens S, Van Looveren R, Loopmans S, Bultynck G, Vinckier S, *et al*: HIF-1α metabolically controls collagen synthesis and modification in chondrocytes. Nature 565: 511-515, 2019.
17. Lu C, Saless N, Wang X, Sinha A, Decker S, Kazakia G, Hou H, Williams B, Swartz HM, Hunt TK, *et al*: The role of oxygen during fracture healing. Bone 52: 220-229, 2013.
18. Johnson RW, Sowder ME and Giaccia AJ: Hypoxia and bone metastatic disease. Curr Osteoporos Rep 15: 231-238, 2017.
19. An Y, Liu WJ, Xue P, Ma Y, Zhang LQ, Zhu B, Qi M, Li LY, Zhang YJ, Wang QT and Lin Y: Autophagy promotes MSC-mediated vascularization in cutaneous wound healing via regulation of VEGF secretion. Cell Death Dis 9: 58, 2018.

20. Schipani E, Ryan HE, Didrickson S, Kobayashi T, Knight M and Johnson RS: Hypoxia in cartilage: HIF-1alpha is essential for chondrocyte growth arrest and survival. Genes Dev 15: 2865-2876, 2001.
21. Provot S and Schipani E: Fetal growth plate: A developmental model of cellular adaptation to hypoxia. Ann N Y Acad Sci 1117: 26-39, 2007.
22. Chakraborty AA, Laukka T, Myllykoski M, Ringel AE, Booker MA, Tolstorukov MY, Meng YJ, Meier SR, Jennings RB, Creech AL, *et al*: Histone demethylase KDM6A directly senses oxygen to control chromatin and cell fate. Science 363: 1217-1222, 2019.
23. Tamagawa H, Fujii M, Togasaki K, Seino T, Kawasaki S, Takano A, Toshimitsu K, Takahashi S, Ohta Y, Matano M, *et al*: Wnt-deficient and hypoxic environment orchestrates squamous reprogramming of human pancreatic ductal adenocarcinoma. Nat Cell Biol 26: 1759-1772, 2024.
24. Kong N, Zhang R, Wu G, Sui X, Wang J, Kim NY, Blake S, De D, Xie T, Cao Y and Tao W: Intravesical delivery of KDM6A-mRNA via mucoadhesive nanoparticles inhibits the metastasis of bladder cancer. Proc Natl Acad Sci USA 119: e2112696119, 2022.
25. Wang JJ, Wang X, Xian YE, Chen ZQ, Sun YP, Fu YW, Wu ZK, Li PX, Zhou ES and Yang ZT: The JMJD3 histone demethylase inhibitor GSK-J1 ameliorates lipopolysaccharide-induced inflammation in a mastitis model. J Biol Chem 298: 102017, 2022.
26. Gao M, Li Y, Cao P, Liu H, Chen J and Kang S: Exploring the therapeutic potential of targeting polycomb repressive complex 2 in lung cancer. Front Oncol 13: 1216289, 2023.
27. De Santa F, Totaro MG, Prosperini E, Notarbartolo S, Testa G and Natoli G: The histone H3 lysine-27 demethylase Jmjd3 links inflammation to inhibition of polycomb-mediated gene silencing. Cell 130: 1083-1094, 2007.
28. Lee S, Lee JW and Lee SK: UTX, a histone H3-lysine 27 demethylase, acts as a critical switch to activate the cardiac developmental program. Dev Cell 22: 25-37, 2012.
29. Thieme S, Gyárfás T, Richter C, Özhan G, Fu J, Alexopoulou D, Muders MH, Michalk I, Jakob C, Dahl A, *et al*: The histone demethylase UTX regulates stem cell migration and hematopoiesis. Blood 121: 2462-2473, 2013.
30. Hemming S, Cakouros D, Isenmann S, Cooper L, Menicanin D, Zannettino A and Gronthos S: EZH2 and KDM6A act as an epigenetic switch to regulate mesenchymal stem cell lineage specification. Stem Cells 32: 802-815, 2014.
31. Pribadi C, Cakouros D, Camp E, Anderson P and Gronthos S: KDM6A-mediated regulation of cranial frontal bone suture fusion in mice is sex dependent. Stem Cells Dev 32: 398-409, 2023.
32. Wise JK, Sena K, Vranizan K, Pollock JF, Healy KE, Hughes WF, Sumner DR and Virdi AS: Temporal gene expression profiling during rat femoral marrow ablation-induced intramembranous bone regeneration. PLoS One 5: e12987, 2010.
33. Teng JW, Ji PF and Zhao ZG: MiR-214-3p inhibits β-catenin signaling pathway leading to delayed fracture healing. Eur Rev Med Pharmacol Sci 22: 17-24, 2018.
34. Zhou J, Liu HX, Li SH, Gong YS, Zhou MW, Zhang JH and Zhu GY: Effects of human umbilical cord mesenchymal stem cells-derived exosomes on fracture healing in rats through the Wnt signaling pathway. Eur Rev Med Pharmacol Sci 23: 4954-4960, 2019.
35. Yao CJ, Lv Y, Zhang CJ, Jin JX, Xu LH, Jiang J, Geng B, Li H, Xia YY and Wu M: MicroRNA-185 inhibits the growth and proliferation of osteoblasts in fracture healing by targeting PTH gene through down-regulating Wnt/β-catenin axis: In an animal experiment. Biochem Biophys Res Commun 501: 55-63, 2018.
36. Zhou H, Zhang L, Chen Y, Zhu CH, Chen FM and Li A: Research progress on the hedgehog signalling pathway in regulating bone formation and homeostasis. Cell Prolif 55: e13162, 2022.
37. Minear S, Leucht P, Jiang J, Liu B, Zeng A, Fuerer C, Nusse R and Helms JA: Wnt proteins promote bone regeneration. Sci Transl Med 2: 29ra30, 2010.
38. Suen PK, He YX, Chow DHK, Huang L, Li C, Ke HZ, Ominsky MS and Qin L: Sclerostin monoclonal antibody enhanced bone fracture healing in an open osteotomy model in rats. J Orthop Res 32: 997-1005, 2014.
39. Florio M, Gunasekaran K, Stolina M, Li X, Liu L, Tipton B, Salimi-Moosavi H, Asuncion FJ, Li C, Sun B, *et al*: A bispecific antibody targeting sclerostin and DKK-1 promotes bone mass accrual and fracture repair. Nat Commun 7: 11505, 2016.
40. Jin H, Wang B, Li J, Xie W, Mao Q, Li S, Dong F, Sun Y, Ke HZ, Babij P, *et al*: Anti-DKK1 antibody promotes bone fracture healing through activation of β-catenin signaling. Bone 71: 63-75, 2015.
41. Houben A, Kostanova-Poliakova D, Weissenböck M, Graf J, Teufel S, von der Mark K and Hartmann C: β-catenin activity in late hypertrophic chondrocytes locally orchestrates osteoblastogenesis and osteoclastogenesis. Development 143: 3826-3838, 2016.
42. Meng Y, Zhang T, Zheng R, Ding S, Yang J, Liu R, Jiang Y and Jiang W: Depletion of demethylase KDM6 enhances early neuroectoderm commitment of human PSCs. Front Cell Dev Biol 9: 702462, 2021.
43. Kikuchi K, Haneda M, Hayashi S, Maeda T, Nakano N, Kuroda Y, Tsubosaka M, Kamenaga T, Fujita M, Ikuta K, *et al*: P21 deficiency exhibits delayed endochondral ossification during fracture healing. Bone 165: 116572, 2022.
44. Catheline SE, Hoak D, Chang M, Ketz JP, Hilton MJ, Zuscik MJ and Jonason JH: Chondrocyte-specific RUNX2 overexpression accelerates post-traumatic osteoarthritis progression in adult mice. J Bone Miner Res 34: 1676-1689, 2019.
45. Gao H, Huang J, Wei Q and He C: Advances in animal models for studying bone fracture healing. Bioengineering (Basel) 10: 201, 2023.
46. Ramírez-Salazar EG, Almeraya EV, López-Perez TV, Patiño N, Salmeron J and Velázquez-Cruz R: MicroRNA-548-3p overexpression inhibits proliferation, migration and invasion in osteoblast-like cells by targeting STAT1 and MAFB. J Biochem 168: 203-211, 2020.
47. Cheng Z, Li A, Tu CL, Maria CS, Szeto N, Herberger A, Chen TH, Song F, Wang J, Liu X, *et al*: Calcium-sensing receptors in chondrocytes and osteoblasts are required for callus maturation and fracture healing in mice. J Bone Miner Res 35: 143-154, 2020.
48. Livak KJ and Schmittgen TD: Analysis of relative gene expression data using real-time quantitative PCR and the 2(-Delta Delta C(T)) method. Methods 25: 402-408, 2001.
49. Peyrin F, Dong P, Pacureanu A and Langer M: Micro- and nano-CT for the study of bone ultrastructure. Curr Osteoporos Rep 12: 465-474, 2014.
50. Wang C, Brisson BK, Terajima M, Li Q, Hoxha K, Han B, Goldberg AM, Sherry Liu X, Marcolongo MS, Enomoto-Iwamoto M, *et al*: Type III collagen is a key regulator of the collagen fibrillar structure and biomechanics of articular cartilage and meniscus. Matrix Biol 85-86: 47-67, 2020.
51. Chen M, Zhu X, Zhang L and Zhao D: COL5A2 is a prognostic-related biomarker and correlated with immune infiltrates in gastric cancer based on transcriptomics and single-cell RNA sequencing. BMC Med Genomics 16: 220, 2023.
52. Wang L, Chen S, Zhang H, Wei G, Ma F, Zhang M, Zhang B, Yang S, Cheng H, Yang R, *et al*: Serine protease inhibitor E2 protects against cartilage tissue destruction and inflammation in osteoarthritis by targeting NF-κB signalling. Rheumatology (Oxford) 63: 3172-3183, 2024.
53. Chen YH, Xu NZ, Hong C, Li WQ, Zhang YQ, Yu XY, Huang YL and Zhou JY: Myo1b promotes tumor progression and angiogenesis by inhibiting autophagic degradation of HIF-1α in colorectal cancer. Cell Death Dis 13: 939, 2022.
54. Shi B, Li W, Song Y, Wang Z, Ju R, Ulman A, Hu J, Palomba F, Zhao Y, Le JP, *et al*: UTX condensation underlies its tumour-suppressive activity. Nature 597: 726-731, 2021.
55. Wen Y, Chen X, Feng H, Wang X, Kang X, Zhao P, Zhao C and Wei Y: Kdm6a deficiency in microglia/macrophages epigenetically silences Lcn2 expression and reduces photoreceptor dysfunction in diabetic retinopathy. Metabolism 136: 155293, 2022.
56. Yang D, Okamura H, Teramachi J and Haneji T: Histone demethylase Utx regulates differentiation and mineralization in osteoblasts. J Cell Biochem 116: 2628-2636, 2015.
57. Duplaquet L, Li Y, Booker MA, Xie Y, Olsen SN, Patel RA, Hong D, Hatton C, Denize T, Walton E, *et al*: KDM6A epigenetically regulates subtype plasticity in small cell lung cancer. Nat Cell Biol 25: 1346-1358, 2023.
58. Yang Y, Chen C, Zuo Q, Lu H, Salman S, Lyu Y, Huang TYT, Wicks EE, Jackson W III, Datan E, *et al*: NARF is a hypoxia-induced coactivator for OCT4-mediated breast cancer stem cell specification. Sci Adv 8: eabo5000, 2022.
59. Li H, Liu Y, Wang Y, Zhao X and Qi X: Hormone therapy for ovarian cancer: Emphasis on mechanisms and applications (Review). Oncol Rep 46: 223, 2021.